Monthly Notices
of the
ROYAL ASTRONOMICAL SOCIETY

MNRAS **440,** 3588–3612 (2014) doi:10.1093/mnras/stu493

The pros and cons of the inversion method approach to derive 3D dust emission properties in the ISM: the Hi-GAL field centred on $(l, b) = (30°, 0°)$

A. Traficante,[1,2,3★] R. Paladini,[3] M. Compiegne,[3,4] M. I. R. Alves,[1,5] L. Cambrésy,[6] S. J. Gibson,[7] C. T. Tibbs,[3] A. Noriega-Crespo,[3] S. Molinari,[8] S. J. Carey,[3] J. G. Ingalls,[3] P. Natoli,[9,10,11] R. D. Davies,[1] R. J. Davis,[1] C. Dickinson[1] and G. A. Fuller[1]

[1]*Jodrell Bank Centre for Astrophysics, School of Physics and Astronomy, The University of Manchester, Oxford Road, Manchester M13 9PL, UK*
[2]*Dipartimento di Fisica, Università di Roma Tor Vergata, I-00133 Italy*
[3]*Infrared Processing Analysis Center, California Institute of Technology, Pasadena, CA 91125, USA*
[4]*Laboratoire d'Optique Atmospherique, UMR8518, CNRS-INSU, Université Lille 1, France*
[5]*Institut d'Astrophysique Spatiale, CNRS (UMR8617) Universite' Paris-Sud 11, F-91405 Orsay, France*
[6]*Observatoire astronomique de Strasbourg, Université de Strasbourg, CNRS, UMR 7550, France*
[7]*Department of Physics & Astronomy, Western Kentucky University, Bowling Green, KY 42101, USA*
[8]*INAF, Istituto Fisica Spazio Interplanetario, I-00133 Rome, Italy*
[9]*Dipartimento di Fisica e Scienze della Terra, Università di Ferrara e Sezione INFN Ferrara, Via Saragat 1, I-44122 Ferrara, Italy*
[10]*Agenzia Spaziale Italiana Science Data Center, c/o ESRIN, via Galileo Galilei, I-00044 Frascati, Italy*
[11]*INAF/IASF Bologna, Via Gobetti 101, I-40129 Bologna, Italy*

Accepted 2014 March 12. Received 2014 February 14; in original form 2012 June 22

ABSTRACT

Herschel far-infrared continuum data obtained as part of the Hi-GAL survey have been used, together with the GLIMPSE 8 μm and MIPSGAL 24 μm data, to attempt the first 3D-decomposition of dust emission associated with atomic, molecular and ionized gas at 15 arcmin angular resolution. Our initial test case is a 2 × 2 square degrees region centred on $(l, b) = (30^\circ, 0^\circ)$, a direction that encompasses the origin point of the Scutum–Crux Arm at the tip of the Galactic Bar. Coupling the IR maps with velocity maps specific for different gas phases (H I 21cm, ^{12}CO and ^{13}CO, and radio recombination lines), we estimate the properties of dust blended with each of the gas components and at different Galactocentric distances along the line of sight (LOS). A statistical Pearson's coefficients analysis is used to study the correlation between the column densities estimated for each gas component and the intensity of the IR emission. This analysis provides evidence that the 2 × 2 square degree field under consideration is characterized by the presence of a gas component not accounted for by the standard tracers, possibly associated with warm H_2 and cold H I. We demonstrate that the IR radiation in the range $8 < \lambda < 500$ μm is systematically dominated by emission originating within the Scutum–Crux Arm. By applying an inversion method, we recover the dust emissivities associated with atomic, molecular and ionized gas. Using the DustEM model, we fit the spectral energy distributions for each gas phase, and find average dust temperatures of $T_{\rm d,H\,I} = 18.82 \pm 0.47$ K, $T_{\rm d,H_2} = 18.84 \pm 1.06$ K and $T_{\rm d,H\,II} = 22.56 \pm 0.64$ K, respectively. We also obtain an indication for polycyclic aromatic hydrocarbons depletion in the *diffuse* ionized gas. We demonstrate the importance of including the ionized component in 3D-decompositions of the total IR emission. However, the main goal of this work is to discuss the impact of the missing column density associated with the *dark gas* component on the accurate evaluation of the dust properties, and to shed light on the limitations of the inversion method approach when this is applied to a small section of the Galactic plane and when the working resolution allows sufficient de-blending of the gas components along the LOS.

Key words: dust, extinction – Galaxy: structure – infrared: ISM.

★ E-mail: alessio.traficante@manchester.ac.uk

1 INTRODUCTION

A variety of space-borne experiments in the course of the last two decades (*IRAS*, *Spitzer*, *Herschel*) have shown that the Galaxy is filled with relatively cold dust ($15 \leq T_{\rm d} \leq 30$ K, e.g. Ferrière 2001) distributed along each line of sight (LOS), and associated with the atomic, molecular and ionized gas phases. This finding has also been recently confirmed by the *Planck* whole-sky observations (Planck Collaboration 2011d,e,f,g).

Dust grains can absorb and re-emit a large fraction of the radiation provided by stellar sources. Depending on the size, they are stochastically heated (i.e. the smaller grains, which emit mainly in the near/mid-IR), or reach thermal equilibrium (i.e. the bigger grains, which emit predominantly in the far-IR regime).

Dust emission properties have been intensely studied at high Galactic latitudes, where each gas phase can be assumed relatively isolated from the others, and mixing along the LOS can be avoided (e.g. Boulanger & Perault 1988; Boulanger et al. 1996; Lagache et al. 2000). On the contrary, in the Galactic plane disentangling dust emission arising from different gas components and intrinsically different environments is a complicated problem, which requires additional kinematic information on the emitting gas (e.g. Bloemen, Deul & Thaddeus 1990).

The separation can be achieved with the so-called *inversion method*, originally introduced by Bloemen et al. (1986) to analyse the individual contribution of atomic and molecular gas to the integrated γ-ray emission. The model was later extended by Bloemen et al. (1990) to include the far-infrared (FIR) emission across the Galactic plane observed with *IRAS* at 60 and 100 μm. So far, the application of the inversion method has been limited by the angular resolution of the available IR and ancillary data (equal or close to 1°), which does not allow us to, e.g., spatially separate individual clouds (Bloemen et al. 1990; Giard et al. 1994; Sodroski et al. 1997; Paladini et al. 2007; Planck Collaboration 2011c). These works have demonstrated that, on average, most of the Galactic IR luminosity is associated with dust in the atomic gas component, which is primarily irradiated by the local radiation field. Dust associated with the molecular and ionized components, on the other hand, is mostly heated by O and B stars embedded in molecular clouds (Sodroski et al. 1997; Paladini et al. 2007). Planck Collaboration (2011c) decomposed the emission from 12 μm to millimetre wavelengths using *IRAS*, *COBE*-DIRBE, *WMAP* and the recent *Planck* data in the latitude range $|b| \leq 10^\circ$ and found evidence of the existence of a significant amount of cold atomic and warm molecular gas not accounted for by the standard tracers. This gas is typically referred to as *dark gas* (Grenier, Casandjian & Terrier 2005). In particular, the authors of this work claim that the *dark gas* column density is comparable to – or greater than – the column density of molecular gas outside the Molecular Ring, i.e. a region of the Galaxy comprised between Galactocentric radius $4\,{\rm kpc} < R < 8\,{\rm kpc}$, where 70 per cent of the molecular gas resides (Combes 1991).

As well as using low-spatial resolution, early inversion works often did not include the ionized gas component, as historically its contribution to the overall IR emission was thought to be negligible (Bloemen et al. 1990; Giard et al. 1994). A few studies (Sodroski et al. 1997; Paladini et al. 2007; Planck Collaboration 2011c) did take this phase of the gas into account, but used the only available data at the time for tracing ionized gas, that is radio continuum data. There are two problems with this approach. The first is that radio continuum emission is not uniquely associated with the interaction – and deceleration – of free electrons with ions in a plasma, the free–free or bremsstrahlung emission: at low frequencies (5 GHz or less), one has to estimate and subtract a possible contamination due to synchrotron emission (e.g. Paladini et al. 2005), while at relatively high frequencies (>10 GHz), spinning dust emission may become significant (e.g. Planck Collaboration 2011b,c). The second, even more important, issue is the fact that radio continuum data are unable to provide the 3D-information on the location of the emitting gas which is required by inversion techniques.

The work we describe in this paper is therefore motivated by the following considerations.

(i) The resolution and sensitivity of the newly available *Spitzer* and *Herschel* data dramatically improve our view of the Galactic plane at IR wavelengths: the combined GLIMPSE (Benjamin et al. 2003), MIPSGAL (Carey et al. 2009) and Hi-GAL (Molinari et al. 2010) surveys have mapped the inner Galactic plane in the wavelength range $8\,\mu{\rm m} \leq \lambda \leq 500\,\mu{\rm m}$ with a resolution of 35 arcsec, or higher. These new data allow us to set more stringent constraints on dust properties and on their variations with Galactocentric radius.

(ii) The last couple of years have witnessed a tremendous improvement in the quality of available data on the ionized gas. In particular, hydrogen recombination lines (RRLs) have been observed for large portions of the Galactic plane (Staveley-Smith et al. 1996; Alves et al. 2012). These data are sampled with a resolution of ≃15 arcmin, which allows us to work with an ∼4 times better resolution than the previous inversions. Even more important, they provide unprecedented information about the properties and distribution of the ionized gas component along the LOS.

(iii) In previous inversion works, the decomposition into Galactocentric bins has been done *blindly*, that is, without taking into account local features present at a given location of the Galaxy or on specific angular scales. The higher resolution of the IR as well as of the ancillary data allow now a more targeted approach.

(iv) Last but not least, if on one side the higher angular resolution of the available data makes it possible to devote more attention to the specific content of the Galactic region to *invert*, on the other hand it sheds light on the limitations of the inversion technique itself. Hence, one of the goals of this work is to investigate and describe these limitations.

In this first paper, we concentrate on a $2^\circ \times 2^\circ$ field centred on $(l, b) = (30.^\circ0, 0.^\circ0)$ observed by the GLIMPSE, MIPSGAL and Hi-GAL surveys. This field was one of two observed during the Hi-GAL Science Demonstration Phase (SDP). Therefore, hereafter we will refer to it as SDPF1 (*Science Demonstration Phase Field 1*).

The paper is organized as follows. A review of the content of SDPF1 is presented in Section 2. The IR and ancillary radio data used for the analysis are described in Section 3. The inversion model is discussed in Section 4, as well as the Galactocentric region subdivision and the gas column density evaluation for each gas phase. We find evidence of untraced cold atomic and possibly warm molecular gas features extending up to several arcminutes. These features do not allow a correct evaluation of the gas column densities, thereby preventing the inversion model from working properly. The regions where these features are dominant, however, can be predicted by analysing the correlation between the gas column densities and the IR maps, as explained in Section 5. In Section 6, we present our results, and discuss the limitations of the inversion model in its current stage of development. We also investigate the importance of accounting for dust associated with the ionized gas, by demonstrating with a simple test the erroneous conclusions that one may reach by neglecting this component. In Section 7, we describe our conclusions.

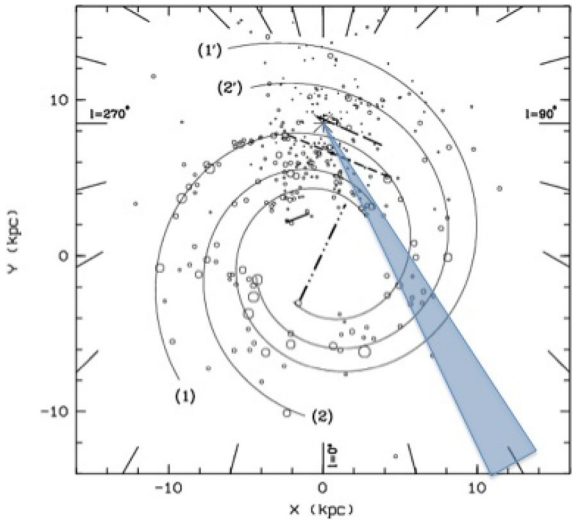

Figure 1. Superposition of the $l = 30^\circ$ LOS with the Russeil (2003) Galactic model. The circles represent the star-forming complexes used by the author to estimate the Galactic spiral arm pattern. The best-fitting model has four arms. 1: Sagittarius–Carina Arm; 2: Scutum–Crux Arm; 1 arcmin: Norma–Cygnus Arm; 2 arcmin: Perseus Arm. A star denotes the position of the Sun. The $l = 30^\circ$ LOS is tangent to the Scutum–Crux Arm. The short dashed line, which passes through the $l = 30^\circ$ LOS, is the expected departure from a logarithmic spiral arm observed for the Sagittarius–Carina Arm. More information about the model can be found in Russeil (2003).

2 THE CONTENT OF SDPF1

According to the Russeil (2003) model of the Galactic spiral structure, SDPF1 intercepts the Sagittarius Arm twice, and both the Norma–Cygnus Arm and the Perseum Arm once (Fig. 1). Furthermore, the LOS also cuts through the Scutum–Crux Arm at the tangent point which, adopting a Sun–Galactic Centre distance of 8.5 kpc, is found at a Galactocentric distance $R = 4.25$ kpc. Both the source content and local interstellar medium (ISM) of SDPF1 have been extensively investigated (see Fig. 2).

The mini-starbust complex W43, located near $l = 30.^\circ8$ (Bally et al. 2010), is the brightest source in the field and one of the brightest FIR sources in the entire Galaxy. It is located at $d \simeq 5.5$ kpc, corresponding to a Galactocentric distance $R \simeq 4.65$ kpc. This giant H II region contains a cluster of OB and Wolf–Rayet stars and its FIR continuum luminosity is $\sim 3.5 \times 10^6$ $L_\odot$ (Smith, Biermann & Mezger 1978).

An additional 29 H II regions are located in SDPF1 (Anderson & Bania 2009), most of which are evolved (Paladini et al. 2012). Towards the centre of the field is located the well-studied ultracompact H II region G29.944−0.04 (Quireza et al. 2006). The N49 H II bubble, centred on $(l,b) = (28.^\circ83, -0.^\circ23)$, is a known case of triggering scenario (Zavagno et al. 2010). Two separate H II regions forming the RCW175 group and located towards the edge of the field at $(l, b) = (29.^\circ07, -0.^\circ68)$ exhibit spinning dust emission (Tibbs et al. 2012).

About 50 molecular clouds sit in the proximity of W43, and a giant cloud with a diameter of ∼20 pc surrounds W43 itself (Bally et al. 2010, and references therein). In total, ∼75 molecular clouds

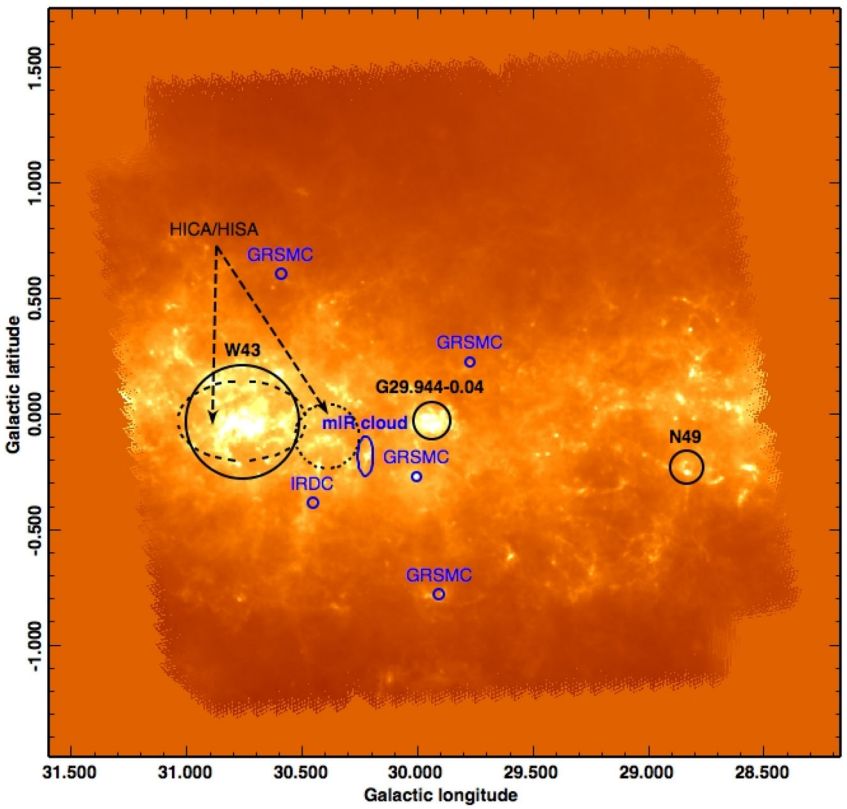

Figure 2. Hi-GAL 500 μm data for SDPF1. The black circles represent W43, G29.944−0.04 and N49. The blue circles denote a subsamples of the ∼75 molecular clouds found in SDPF1, as well as one of the most prominent IRDCs catalogued by Peretto & Fuller (2009) and an example of a mid-IR bright and mid-IR dark cloud studied by Battersby et al. (2011) in these 2 × 2 square degrees. Finally, the black-dotted circles indicate H I absorption features, a combination of HICA and HISA (see Section 2 for details).

can be found in SDPF1 (Rathborne et al. 2009, see Fig. 2), together with ∼340 infrared dark clouds (IRDCs) from the Peretto & Fuller (2009) catalogue.

A cold layer of atomic hydrogen (Gibson et al. 2004) has also been observed in SDPF1. As discussed in Section 6.2, this layer is seen in absorption in the H I 21 cm line. It is composed of a combination of H I Self-Absorption features (HISA; e.g. Gibson 2010), which require a warmer background provided by H I itself, and H I Continuum Absorption features (HICA; Strasser & Taylor 2004), which instead require a continuum background. The most relevant features are seen in correspondence of W43.

A detailed investigation of the properties of the ISM in SDPF1 is presented in Bernard et al. (2010). By comparing the Hi-GAL maps with a 3D-extinction map, these authors find that dust temperature is higher when the LOS intercepts the spiral arms. The relation between dust emissivity spectral index β and dust temperature $T_{\rm d}$ is instead analysed by Paradis et al. (2010), by combining Hi-GAL and *IRAS* data. Evidence for a $T_{\rm d} - \beta$ anticorrelation is reported in their work, although the authors caution against possible spurious effects due to temperature mixing along the LOS.

3 IR AND ANCILLARY RADIO DATA

In this section, we describe the input IR data and the ancillary radio data used to trace the different gas phases.

3.1 IR data

We consider IR imaging data at seven different wavelengths covering the range $8\,\mu{\rm m} \leq \lambda \leq 500\,\mu{\rm m}$. From the GLIMPSE and MIPSGAL surveys, we use the 8 and 24 μm data, respectively. The map resolution is 2 arcsec for GLIMPSE 8 μm and 6 arcsec for MIPSGAL 24 μm. Details of the data reduction can be found in Benjamin et al. (2003) and in Carey et al. (2009) for GLIMPSE and MIPSGAL, respectively. At longer wavelengths, we use data from the Hi-GAL survey, which has mapped the whole Galactic plane in five bands in the range $70\,\mu{\rm m} \leq \lambda \leq 500\,\mu{\rm m}$. The first Hi-GAL survey covers almost 280 square degrees of the inner Galaxy, with a 2° wide strip centred on the Galactic plane in the longitude range $|l| \leq 70°$. The scanning strategy of the survey is organized in tiles of 2 × 2 square degrees. During the *Herschel* SDP two Hi-GAL tiles were observed, the SDPF1 field studied in this work and another, which also covers 2 × 2 square degrees, centred on $(l, b) = (59°, 0°)$. The data have been taken with both the PACS (Poglitsch et al. 2010) and SPIRE (Griffin et al. 2010) instruments in parallel mode and are reduced with the ROMAGAL pipeline (Traficante et al. 2011). PACS has observed the sky at 70 and 160 μm, while SPIRE at 250 , 350 and 500 μm. The Hi-GAL spatial resolution is ≃10 and ≃13.5 arcsec for PACS and 18, 24 and 34.5 arcsec for SPIRE (Traficante et al. 2011). The zero-level offsets in the Hi-GAL maps are evaluated as described in Bernard et al. (2010).

The seven maps are point-source subtracted in order to avoid contamination at high spatial frequencies. Point sources were identified and removed by using two software tools, one tailored for *Spitzer* and the other for *Herschel*. For the *Spitzer* data, i.e. IRAC 8 μm and MIPS 24 μm, we used the Spitzer Science Center APEX package (Makovoz & Marleau 2005) under the MOPEX tools.[1] For the *Herschel* data, for which we had to build our own point spread functions from the data itself, we used 'STARFINDER'[2] (Diolaiti et al. 2000). In both cases, the removal is carried out in such a way that the residuals from the point-source subtraction match as close as possible the noise properties of the original images.

The seven IR maps are shown in Fig. D1.

3.2 Ancillary data

3.2.1 *Atomic hydrogen*

The atomic gas phase (H I) is traced with the 21 cm line, which can be easily detected across the Galaxy (Stil et al. 2006). We used the VLA Galactic Plane Survey (VGPS) data, covering the longitude region $18° \leq l \leq 67°$ for $|b| \leq 1.^\circ3$ up to $|b| \leq 2.^\circ3$ (Stil et al. 2006). These data are part of the International Galactic Plane Survey which includes the VGPS, the Canadian Galactic Plane Survey and the Southern Galactic Plane Survey and covers ∼90 per cent of the 21 cm line Galactic disc emission. The VGPS brightness temperature ($T_{\rm b}$) maps have an angular resolution of 1 arcmin with a velocity resolution of 1.56 km s^{-1}. The survey covers the velocity range $-113 \leq V_{\rm LSR} \leq 167$ km s^{-1}. The rms noise per channel is 1.8 K on average, depending on the location and velocity (Stil et al. 2006).

Since the VGPS 21 cm line data are continuum subtracted, a few pixels in correspondence of bright H II regions have very low (even negative) values due to strong H I continuum emission which arises from the H II regions. In order to identify and flag these pixels, we have used the VGPS continuum data (Stil et al. 2006). We masked the pixels in all velocity channels of the 21 cm data cube with continuum temperature $T_{\rm c} \geq 50$ K. This threshold allows us to mask pixels in correspondence of bright H II regions but without including the cold diffuse regions, which also appear as absorption features in the H I 21 cm data (see Section 6.2). In total, less than 1 per cent of the pixels have been masked, the majority of them in correspondence of W43. The same pixels flagged in the 21 cm data cube were also flagged in the data cubes for the other gas tracers.

3.2.2 *Molecular hydrogen*

The molecular gas (H_2) has no observable transitions under the conditions typical of molecular clouds, but it can be indirectly traced with carbon monoxide (CO) emission. H_2 is primarily traced by measuring the $J = 1 \rightarrow 0$ rotational transition line of the most abundant CO isotope in the Galaxy, ^{12}CO. However, SDPF1 is characterized by the presence of many molecular clouds, IRDCs and H I absorption features (see Section 2). These potentially cold, dense regions are better traced with the $J = 1 \rightarrow 0$ line emitted from ^{13}CO isotope (see Section 4.3.2).

The $J = 1 \rightarrow 0$ lines of ^{12}CO and ^{13}CO used in this work were observed with the Massachusetts-Stony Brook Galactic plane CO survey (UMSB; Sanders et al. 1986) and the Galactic Ring Survey (GRS, Jackson et al. 2006), respectively. Both surveys were carried out with the Boston-FCRAO 14 m telescope. The UMSB survey covers the range $8° \leq l \leq 90°$, $|b| \leq 1.^\circ05$. The spatial resolution is 44 arcsec, even though the sky was sampled with a 3 arcmin step. The pixel size of the map is 3 arcmin, which subsamples the telescope beam and does not preserve the spatial information below this value. In order to alleviate the effect of the under sampling, we first regridded the data to 44 arcsec, and then assigned each

[1] http://irsa.ipac.caltech.edu/data/SPITZER/docs/dataanalysistools/tools/mopex/

[2] http://www.bo.astro.it/StarFinder/paper6.htm

pixel value in the initial map to a pixel in the new map. We then interpolated consecutive pixel values using a cubic interpolation routine, and finally smoothed and re-binned the map to the original 3 arcmin spatial resolution. This approach assures a better continuity in surface brightness across the map. However, we notice that the arcminute structures present in the data are smeared out at our final working resolution of 14.8 arcmin (see Section 4.1), and the results of the analysis do not vary significantly if we do not apply the cubic interpolation step described above.

The spectral resolution is 1 km s^{-1} with an rms sensitivity of 0.4 K per velocity channel.

The GRS has mapped the first quadrant of the Milky Way for $18^\circ \leq l \leq 55.^\circ7$, $|b| \leq 1^\circ$. The sensitivity is $\leq$0.4 K per velocity channel, the spectral resolution is 0.212 km s^{-1} and the angular resolution is 46 arcsec sampled with a 22 arcsec grid.

Since we use both the CO isotopes to evaluate molecular hydrogen column density (see Section 4.3.2), we rebinned the ^{12}CO and ^{13}CO data on the same grid and, using a Gaussian kernel, we convolved both data sets to 9 arcmin. The convolved maps have a pixel size of 3 arcmin, which is the same spatial resolution of the ^{12}CO map and allows us to properly sample the kernel.

3.2.3 Ionized hydrogen

The warm ionized medium (WIM) is generally traced using either free–free continuum emission or optical (e.g. Hα) and radio (RRL) transition lines. In the Introduction, we have already discussed the limitations of using free–free emission in the context of inversion works. Both the Hα line and radio recombination lines (RRLs) are part of the cascade of recombination transitions. However, the Hα line is emitted when a transition occurs between relatively low-quantum levels, i.e. from $n = 3$ to 2, while RRLs correspond to transitions between high quantum levels, with n typically >40. With respect to Hα, RRLs have the advantage of not being affected by dust absorption (e.g. Dickinson, Davies & Davis 2003), thus providing a *clean* view of the ionized gas across the Galaxy.

In this work, to trace H II and evaluate the corresponding column density we make use primarily of RRL data. In particular, we use RRLs corresponding to three different transitions, i.e. H166α, H167α and H168α. These have been observed by the H I Parkes All-Sky Survey (HIPASS; Staveley-Smith et al. 1996) and the associated Zone of Avoidance (ZOA), aimed at detecting galaxies in the local Universe. The integration time of the ZOA survey, 2100 s per beam, is five times higher than that of the HIPASS. The data from the two surveys have been combined and the three RRLs have been stacked to achieve a final rms sensitivity of 3 mK/beam/channel. The beam is 14.8 arcmin, the pixel dimension is set to 4 arcmin and the spectral resolution is 20.0 km s^{-1} (Alves et al. 2012). Details of the data reduction are given in Alves et al. (2010).

We complement the information provided by the RRL data, especially in terms of electron density of the observed ionized gas, with free–free radio continuum data. The free–free data for our region are available from the observations made at 5 GHz (i.e. 6 cm) with the Parkes 64 m telescope (Haynes, Caswell & Simons 1978), digitized by the Max Planck Institute in Bonn.[3] The survey covers the range $-170^\circ \leq l \leq 40^\circ$, $|b| \leq 1.^\circ5$ at an angular resolution of 4.1 arcmin and a sensitivity of around 10 mJy. We apply baseline/offset removal (of 0.1 and 1 K, respectively) and estimate/subtract the synchrotron contribution according to fig. 7 in Paladini et al. (2005).

[3] http://www3.mpifr-bonn.mpg.de/survey.html

4 THE ANALYSIS METHOD

In the following, we describe the inversion method used to disentangle the dust properties in each gas phase and along different Galactocentric positions. The model requires a subdivision of the Galaxy into Galactocentric bins (hereafter referred to as *rings*) and evaluation of the gas column density for each phase (Section 4.3).

4.1 The 3D-inversion model

We follow the prescription of the inversion model of Bloemen et al. (1990) by assuming that dust emissivities vary with Galactocentric distance, thus remaining constant within fixed Galactocentric rings. This working hypothesis, although not entirely true, has yet its foundations in the real-case scenario. For instance, Dunham et al. (2011) find, by comparing the emission at 1.1 mm with that for different transitions [(1,1), (2,2) and (3,3)] of NH_3, that the properties of cold clumps seem to vary as a function almost exclusively of Galactic radius. In our inversion model, we further assume a single dust temperature and gas-to-dust mass ratio, hence a constant emissivity value per H atom, for each gas phase and Galactocentric ring. We emphasize that this hyphothesis implies that dust emits (or absorbs) coherently within each gas phase and Galactocentric ring, thus ignoring local effects which may alter the emissivities along specific LOS, and this is an intrinsic limitation of the model. Under these assumptions, however, we can express the IR emission at a wavelength λ in a pixel j, $I^j(\lambda)$, as a linear combination of gas column densities and dust emissivities associated with each gas phase in each ring i

$$I^j(\lambda) = \sum_{i=1}^{n} \epsilon_{\rm H\,I}(\lambda, R_i) N^j_{\rm H\,I}(R_i) + \epsilon_{\rm H_2}(\lambda, R_i) N^j_{\rm H_2}(R_i) + \epsilon_{\rm H\,II}(\lambda, R_i) N^j_{\rm H\,II}(R_i). \quad (1)$$

In the expression above, ϵ_α are the dust emissivities (in units of MJy sr^{-1}/10^{20} atoms) for the three gas phases [$\alpha = ({\rm H\,I}, {\rm H_2}, {\rm H\,II})$] in each ring R_i, and N^j_α are the corresponding column densities in pixel j. The summation is taken over the n rings adopted for the decomposition. Once the gas column densities have been evaluated for each ring, the model allows us to disentangle the fraction of the integrated IR emission which is generated within each ring and gas phase, and to estimate the corresponding dust emissivities by solving equation (1) with a least-squares fit analysis.

The column density for each gas component and ring is convolved with a Gaussian kernel at the lowest available resolution, 14.8 arcmin (the RRL data resolution), and the maps rebinned with a pixel scale of 4 arcmin. We note that this spatial resolution is four times higher than in previous inversion works ($\simeq 1^\circ$). Due to the reduced size of the region under investigation (4 square degrees), the number of available pixels that we can use to estimate the dust emissivities is only $\sim$700 (i.e. a factor $\sim 10^2$–10^3 lower with respect to, e.g., Paladini et al. 2007; Planck Collaboration 2011c). Since the error bars associated with the emissivities in our model are estimated with a bootstrap procedure, a small number of samples induces an increase of the random sampling errors arising from the bootstrap method itself (Efron 1979). In Section 6.5, we will show that, if we do not include in the inversion matrix the RRL data, we can afford working with a smaller pixel size, although at the expense of not being able to correctly account for the contribution of dust emission associated with the ionized medium.

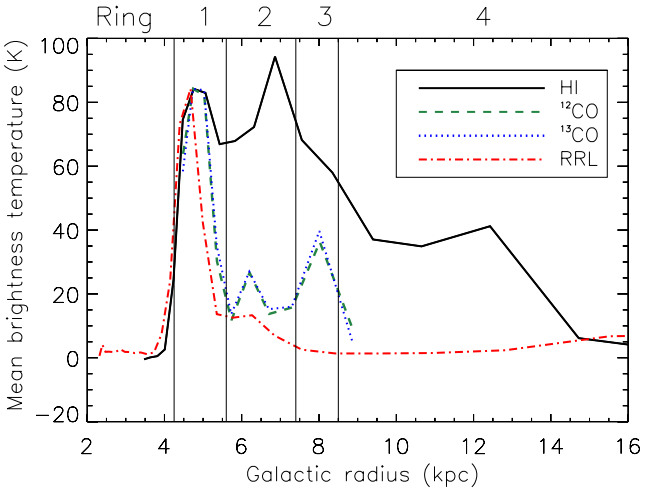

Figure 3. Mean brightness temperature, as a function of Galactocentric radius, for H I (solid line), ^{12}CO (dashed line), ^{13}CO (dotted line) and RRLs (dash–dotted line), respectively. Each data cube has been rebinned to the same velocity resolution, namely 20.0 km s^{-1}. For each gas phase and velocity channel, a median brightness temperature has been computed. All data sets are normalized to the amplitude of the first H I peak. The boundaries of the Galactocentric rings are $R = [4.25, 5.6, 7.4, 8.5, 16.0]$ kpc.

Noteworthy, the IDL[4] code which evaluates the gas column densities and solves equation (1) is based on the code of Paladini et al. (2007). The code has been fully re-designed and now only takes $\simeq$4 min to complete the inversion of a $2^\circ \times 2^\circ$ Hi-GAL tile, rather than $\simeq$100 min required by the old version. The test has been performed on an Intel Core 2 Duo at 2.2 GHz. This code optimization turned out to be critical for this work, as it allowed us to test a large number of model configurations.

4.2 Selection of Galactocentric rings

Fig. 3 presents the median brightness temperature T_b values for each gas tracer as a function of the Galactocentric radius. Radial velocities are converted into Galactocentric distances by applying the Fich, Blitz & Stark (1989) rotation curve and by assuming that the circular motion is the dominant component of velocity. With this assumption, the emission at a particular radial velocity increment translates identically to emission at a single Galactocentric bin. We note also that since the Galactocentric distance is a function of the radial velocities and of the longitude (see the Fich et al. 1989 model), some velocity channels can have part of the emission belonging to one ring and part of it that belongs to the subsequent ring. The longitude value that determines the separation is in correspondence of the Galactocentric distance equal to the ring edges.

In order to allow comparison among different data sets, all data cubes have been rebinned with the RRL velocity resolution, i.e. 20.0 km s^{-1}. In addition, the mean profiles for each gas phase have been normalized to the peak in the first Galactocentric ring of the H I profile.

From Fig. 3, we see that H I has two prominent peaks, one at $R \simeq 5$ kpc and the other at $R \simeq 7$ kpc. There is no clear correlation between H I emission and spiral arms pattern in our Galaxy (e.g. Gibson et al. 2005); however, the first peak is likely due to emission from the Scutum–Crux Arm, being located at the tangent point (see Fig. 1). H I data can be used to trace the Galactic edge up to distances of $\sim$20–25 kpc from the Galactic Centre, depending on the LOS (e.g. Weaver & Williams 1974). In our case, we truncate the H I data to $R = 16$ kpc since, beyond this value, the S/N drops significantly.

The molecular gas peaks at approximately $R \simeq 4.5$ and 8 kpc. The first peak falls in correspondence of the Scutum–Crux Arm. The second peak in CO data is either produced by H_2 located in the local Sagittarius–Carina Arm or, alternatively, in the interarm region between the Sagittarius–Carina Arm (at the second passage through the $l = 30^\circ$ LOS) and the Perseus Arm. It is commonly accepted that interarm regions, despite being characterized by an average gas density $\sim$3.6 lower than the spiral arms (Ferrière 2001), are not devoid of molecular gas. We truncate both the ^{12}CO and ^{13}CO data at $R \simeq 8.5$ kpc since the H_2 column density is known to drop off rapidly beyond $R = R_\odot$ (e.g. Combes 1991; Ferrière 2001).

RRL data also peak around $R \simeq 4.5 - 5$ kpc, in the Scutum–Crux Arm region. This arm contains 80 per cent (i.e. 23 out of a total of 29) of the known H II regions in SDPF1 (Anderson & Bania 2009), including the W43 complex and the bright source G29.944−0.04. This trend mimics the overall radial distribution of ionized medium across the Galaxy (Ferrière 2001). The RRL signal decreases exponentially in the outer Galaxy, being consistent with pure noise at $R \simeq 8.5$ kpc.

To perform the 3D-inversion, we must subdivide the Galaxy into Galactocentric rings by minimizing their cross-correlations. In previous analyses, this step has been performed following a mathematical approach, i.e. using the eigenvalues of the cross-correlation matrix. In our case, we use the physical properties of the gas tracers to guide our decomposition. In Fig. 3, four distinct regions of emission can be clearly identified. The first region (Ring 1, $4.25 \leq R \leq 5.6$ kpc) is characterized by a peak of emission in all tracers (H I, ^{12}CO and ^{13}CO, RRLs) and defines the edges of the Scutum–Crux Arm. The second region (Ring 2, $5.6 \leq R \leq 7.4$ kpc) presents a prominent feature in H I. The third region (Ring 3, $7.4 \leq R \leq 8.5$ kpc) contains significant CO emission and cold H I features (HICA and HISA, see Section 6.2), while H II emission is entirely accounted for by a diffuse component. Finally, region four (Ring 4, $8.5 \leq R \leq 16$ kpc) corresponds to the outer Galaxy and is visible in H I emission only.

4.3 Column density evaluation

In the following, we describe how we evaluate the column densities of each gas phase using the tracers described in Section 3.2.

4.3.1 Atomic hydrogen column density

Due to the blending in SDPF1 of cold and warm H I, the 21 cm line brightness temperature, T_b, in each ring cannot be converted into H I column density, N(H I), with a fixed spin temperature, T_s, following the standard approach of previous inversion works (see e.g. Paladini et al. 2007; Planck Collaboration 2011c). In fact, since in the cold neutral medium $10 \leq T_s \leq 100$ K, and in the warm neutral medium (WNM) T_s ranges from $\sim$500 K to $T_s \sim 5000$ K (e.g. Heiles & Troland 2003; Strasser & Taylor 2004), the assumption of a constant T_s is too simplistic. However, the H I column density can be evaluated by assuming a single emission component in the *optically thin* limit (Dickey & Lockman 1990):

$$N(\mathrm{H\,I})_{\tau \ll 1} \simeq C_0 \int T_b(v)\mathrm{d}v \qquad 10^{20}\ \mathrm{H\ atoms\,cm^{-2}}, \tag{2}$$

where $C_0 = 1.823 \times 10^{18}\ \mathrm{cm^2/(K\,km\,s^{-1})}$. $T_b(v)$ is the observed 21 cm line brightness temperature at the velocity position v. The

[4] Interactive Data Language.

integral is taken over the ensemble of the velocity channels corresponding to each ring. The integrated T_b map in Ring 3 shows an offset around $l = 29.^{\circ}5$ and $l = 30.^{\circ}8$ in correspondence of the longitudes in which some velocity channels have their emission split among Rings 3 and 2. These offsets are present also in Ring 2. However, the steps amount to only a few K and induce a step in column density of $\simeq 1 \times 10^{20}$ H atoms cm^{-2} from the two regions, lower than the mean and the rms value of the map ($\simeq 20 \times 10^{20}$ H atoms cm^{-2} and $\simeq 2.5 \times 10^{20}$ H atoms cm^{-2}, respectively) and in Ring 2 they are not visible (see Fig. D2).

The H I column density evaluated under these hypothesis could underestimate the 'true' column density by a factor of 1.3–1.5, depending on the location (Strasser & Taylor 2004). As a simple test, we tried to rescale the H I column density in each ring by a fixed fraction (the H I column density in each ring has been multiplied by a factor 1.3). The estimated emissivities do not sensibly change from the results showed in Section 6, most likely because the regions in which the assumption of having one component in the optically thin limit fails have their own spatial structure along the LOS.

Since in previous inversion studies the H I column density was evaluated by assuming a fixed spin temperature, we compared the H I column density and dust emissivities for the three phases estimated with the two methods: the optically thin limit and the assumption of a spin temperature. Setting a unique value for the spin temperature is not straightforward. However, considering that T_s has to be higher than the observed T_b, we can fix T_s at the highest T_b value measured along the LOS (e.g. Johannesson et al. 2010). In SDPF1, T_b peaks at $T_b = 160$ K. We then adopt this value to compute N(H I) for all pixels. In doing so, we need to remember that this operation can lead to overestimate T_s in regions far from the peak. The total H I column density estimated with this approach is $\simeq$30 per cent higher than the value obtained in the optically thin limit, with peaks of $\sim$80 per cent for pixels in correspondence of very bright H I emission. Interestingly, such a column density increase is accompanied by a change in morphology of H I emission in the rings. We also run a series of tests adopting a spin temperature in the range $160 \leq T_s \leq 250$ K, following Planck Collaboration (2011c). All these tests show that dust emissivities do not change significantly over this temperature range. Median emissivity differences (for all rings) between the isothermal and optically thin models in H I,H_2 and H II are, respectively, 55, 2 and 8 per cent for $T_s = 160$ K and 29, 3 and 6 per cent for $T_s = 250$ K. In addition, the dust temperature derived from the emissivities using both methods are the same, as is the convergence of the code in different rings (see Section 6), which are the main results of this work.

Both models are not defining accurately the temperature distribution along the LOS, but they are useful to describe a limiting case (the optically thin assumption) or a weighted average (the spin temperature assumption) for obtaining column densities. At the same time, assuming the optically thin condition does not require the evaluation of the optical depth or the spin temperature along the LOS. It represents a well-defined lower limit to the total H I column density, despite the fact that it cannot correctly reproduce the amount of gas along the LOS in cold, dense regions. We therefore decided to apply equation (2) without any further assumptions.

4.3.2 *Molecular hydrogen column density*

The H_2 column density is evaluated in the local thermal equilibrium (LTE) approximation by assuming a constant [CO/H_2] ratio and by using both the ^{12}CO and ^{13}CO isotopes.

In the denser and colder part of the molecular clouds, ^{12}CO becomes optically thick while ^{13}CO can still be considered optically thin. On the other hand, in the external regions of the clouds ^{12}CO is optically thin but ^{13}CO emission is too weak to detect. Thus, we use ^{12}CO where only this isotope is observed, and both ^{13}CO and ^{12}CO otherwise. We emphasize that this approach, although it allows us to better recover the molecular hydrogen column density, is nevertheless affected by some limitations. Noteworthy, CO lines can be self-absorbed, and H_2 cannot be traced in optically thick regions (Pineda, Caselli & Goodman 2008).

For each velocity channel, we searched for pixels where both ^{12}CO and ^{13}CO are detected following these steps:

(1) we compute the median value over all the pixels;
(2) we compute the sigma (σ) with respect to the median;
(3) we isolate the pixels with a value greater than the median value plus 2.5σ in both ^{12}CO and ^{13}CO maps;
(4) we flag the pixels isolated in both maps as common regions.

The sigma evaluated with respect to the median, rather than the mean, assures more stability to fluctuations induced by the signal, especially in channels where bright star-forming regions strongly contribute to the overall emission. The 2.5σ threshold can, in some cases, lead to an inclusion of noisy outliers. A value higher than 2.5σ, however, results in missing pixels where ^{13}CO emission is clearly seen, while a lower value induces the identification of too many outliers. With a threshold of 2.5σ we identify an average of 5 per cent common pixels in each velocity channel, concentrated in the densest regions. Assuming only residual white noise, the outliers are randomly distributed across the map, so the probability that the same outliers are falsely detected in both the ^{12}CO and ^{13}CO maps is <0.1 per cent.

In pixels where only ^{12}CO is observed, T_b is converted into molecular hydrogen column density $N(H_2)$ using the optically thin hypothesis. Then, for a given ring and in each pixel, $N(H_2)$ is proportional to $\int T_b(v)dv$, where the integration is taken over the velocity range corresponding to that ring. We set the conversion factor X_{CO}, which is the ratio of the molecular hydrogen column density (in units 10^{20} H atoms cm^{-2}) to the velocity-integrated CO intensity (K km s^{-1}), equal to 1.8×10^{20} cm^{-2} (K km s^{-1})$^{-1}$, in agreement with the recommended value suggested by Bolatto, Wolfire & Leroy (2013). Recent studies suggest that X_{CO} may vary with metallicity, in particular increasing with Galactocentric distance by a factor 5–10, with an estimated value at $R \simeq 1.5$ kpc of $X_{CO} = 0.3$ (e.g. Strong et al. 2004; Abdo et al. 2010). If this is true, our working hypothesis of $X_{CO} = 1.8$ has the effect of producing an overestimate of the effective molecular gas column densities.

When ^{13}CO is also observed, in order to evaluate the column density, $N(^{13}CO)$, we need to know the excitation temperature T_{ex} and the ^{13}CO optical depth τ_{13} at each velocity v (Duval et al. 2010; Pineda et al. 2010). The details of this analysis are given in Appendix A. $N(^{13}CO)$ is then converted into $N(H_2)$ applying (Stahler & Palla 2005)

$$N(H_2) = 7.5 \times 10^5 \; N(^{13}CO) \qquad (10^{20} \text{ atoms cm}^{-2}). \tag{3}$$

A total of $\sim$27 per cent pixels of the column density maps are observed in both the ^{12}CO and ^{13}CO maps. For $\sim$20 per cent of these common pixels, the estimated column density is $\geq$20 per cent higher than the one calculated with the ^{12}CO data only, confirming the necessity of combining the information, when this is available, from the two isotopes.

4.3.3 *Ionized hydrogen column density*

At low Galactic latitudes, the WIM is characterized by a thin layer which consists of both individual H II regions and diffuse emission (Paladini et al. 2005). RRLs allow us to trace simultaneously these two components.

The RRL brightness temperature peaks in the Scutum–Crux ring where the majority of the H II regions in SDPF1, in particular W43, are located (Fig. 3) and it is significantly low in the other rings. The ionized hydrogen column density, $N(\mathrm{H\,II})$, is proportional to the RRLs brightness temperature, as we are going to show in the following, therefore the H II column density also peaks in Ring 1.

The H II column density can be defined as the mean electron density $\langle n_\mathrm{e}\rangle$ integrated along the LOS:

$$N(\mathrm{H\,II}) = \int \langle n_\mathrm{e}\rangle \mathrm{d}s. \tag{4}$$

The quantity above can be estimated from the emission measure (EM). If we assume along each LOS a standard effective electron density, n_eff:

$$\mathrm{EM} = \int n_\mathrm{e}^2 \mathrm{d}s = n_\mathrm{eff} \times \int \langle n_\mathrm{e}\rangle \mathrm{d}s = n_\mathrm{eff} \times N(\mathrm{H\,II}). \tag{5}$$

EM is evaluated in turn from the integral of the RRL line temperature T_L (Alves et al. 2010):

$$\int T_\mathrm{L} \mathrm{d}\nu = 1.92 \times 10^3 T_\mathrm{e}^{-1.5}\ \mathrm{EM}, \tag{6}$$

where T_e is the mean electron temperature and $\mathrm{d}\nu$ is the frequency interval in kHz. The continuum emission brightness temperature T_b is also proportional to EM (Mezger & Henderson 1967):

$$T_\mathrm{b} = 8.235 \times 10^{-2} a(T_\mathrm{e}) T_\mathrm{e}^{-0.35} \nu_\mathrm{GHz}^{-2.1} (1 + 0.08)\ \mathrm{EM}, \tag{7}$$

where the factor $(1 + 0.08)$ takes into account the additional contribution to T_b from helium, and ν_GHz is the frequency expressed in GHz. Combining this equation with equation (6), we obtain

$$\frac{\int T_\mathrm{L} \mathrm{d}V}{T_\mathrm{b}} = 6.985 \times 10^3 \frac{1}{a(T_\mathrm{e})} \frac{1}{n(\mathrm{He})/[1 + n(\mathrm{H})]} T_\mathrm{e}^{-1.15} \nu_\mathrm{GHz}^{1.1}. \tag{8}$$

In the expression above, $a(T_\mathrm{e})$ is a slowly varying function of T_e and $\mathrm{d}V$ is expressed in km s^{-1}. The factor $n(\mathrm{He})/[1 + n(\mathrm{H})]$ is equivalent to the factor $(1 + 0.08)$ in equation (7).

In order to derive $N(\mathrm{H\,II})$ from equations (5)–(7), we need to know both T_e and n_eff for each of the physical regimes we are considering, that is, H II regions and the diffuse medium. At the RRL data-angular resolution (14.8 arcmin), each of the 29 H II regions in SDPF1 falls within a single pixel, except for the W43 complex. Therefore, apart from W43 which we treat as a special case, we assume that the H II emission in the field originates exclusively in the diffuse emission, thus neglecting the contribution from individual H II regions.

(i) *Mean electron temperature:* for H II regions, T_e is known to increase with Galactocentric radius (e.g. Shaver et al. 1983; Paladini, Davies & De Zotti 2004), varying in the range 4000–8000 K. Alves et al. (2012) have recently shown that the diffuse ionized gas along the Galactic plane has a similar electron temperature of that of H II regions. Therefore, for simplicity, we assume a constant T_e for both W43 and the diffuse H II component and, following Alves et al. (2010), we take $T_\mathrm{e} = 5500$ K.

(ii) *Effective electron density:* in general, n_eff strongly depends on the physical conditions of a given environment. Previous inversion works have often used values close or equal to 10 cm^{-3} (e.g. Paladini et al. 2007; Planck Collaboration 2011c). This value is in agreement with measurements in compact H II regions. In the diffuse ionized medium n_eff is typically lower, i.e. $0.03 < n_\mathrm{eff} < 0.08$ cm^{-3} (e.g. Haffner et al. 2009), especially at intermediate and high Galactic latitudes.

To estimate n_eff for both the diffuse medium in SDPF1 and W43, we use the Parkes 5 GHz data. To this end, we note that the observed free–free emission is proportional to EM and follows equation (7). If we assume that $\langle n_\mathrm{e}\rangle = n_\mathrm{eff}$, it follows that

$$n_\mathrm{eff} = \left(\frac{T_\mathrm{b}}{8.235} \frac{10^2}{a(T_\mathrm{e})} T_\mathrm{e}^{0.35} \nu_\mathrm{GHz}^{2.1} \frac{1}{(1 + 0.08)} \frac{1}{d} \right)^{1/2}, \tag{9}$$

where d is the linear size of the parcel of emitting gas. We emphasize that equation (9) holds true only if the electron density does not vary significantly along the LOS. To ensure that this condition is satisfied, we solve equation (9) independently for W43 and the diffuse medium:

(1) *W43 complex*: in this case, the assumption that the emission is dominated by the star-forming complex with minor contributions from the foreground/background emission is motivated by the fact that T_L in correspondence of the H II region is several orders of magnitudes higher with respect to its surroundings. In the RRL data cube, W43 is at $V_\mathrm{LSR} = 107$ km s^{-1}, which corresponds to a Galactocentric radius of $R \simeq 4.65$ kpc. The complex is known to be on the near side of the Galaxy (Wilson et al. 1970), so its solar distance is $D \simeq 5.5$ kpc, in agreement with Bally et al. (2010). We measure an angular size of $\simeq$29.1 arcmin which, at a distance of 5.5 kpc, is equivalent to an effective size $d \simeq 47.8$ pc. Assuming a spherical geometry, we adopt this value to evaluate n_eff from equation (9). For $T_\mathrm{b} = T_\mathrm{b,W43peak}$, we obtain $n_\mathrm{eff,W43peak} = 43.8$ cm^{-3}.

(2) *Diffuse emission*: for the diffuse component, the definition of the edges of the emitting region is less straightforward. In Section 4.2, we have seen that the emission from H II detected through RRLs drops dramatically beyond $R \simeq 8.5$ kpc. At the far side of the Galaxy the $R \simeq 8.5$ kpc circle intersects $l = 30^\circ$ at a distance of $D \simeq 14.7$ kpc from the Sun. We take this as the outer boundary of the emitting region. To derive n_eff, we then first mask the pixels across the W43 complex, and then compute the median of the values obtained by applying equation (9). The resulting effective electron density is $n_\mathrm{eff,diffuse} = 0.39$ cm^{-3}.

At this stage, in order to obtain a continuous solution, we scale $n_\mathrm{eff,\,W43peak}$ to $n_\mathrm{eff,\,diffuse}$. For this purpose, we use a 2D-Gaussian profile with a full width at half-maximum equal to the measured angular size of W43. Having estimated n_eff, we derive $N(\mathrm{H\,II})$ by combining equations 5, 6 and 8.

4.3.4 *Column density distribution*

We compare the contribution to the total gas column density provided by each ring and obtain that most of the gas (∼65 per cent) is located in Ring 1. Ring 2 accounts for another ∼20 per cent, while the remaining ∼15 per cent is distributed between Rings 3 and 4.

The column density maps for each gas phase and ring are in Figs D2–D4.

5 STATISTICAL CORRELATION ANALYSIS

The inversion model is based on the hypothesis that the total IR emission at a given wavelength can be decomposed into dust emission associated with different gas phases and Galactocentric rings. This hypothesis implies that the integrated IR dust emission at each

given wavelength linearly correlates with the dust emission associated with each gas component and Galactocentric ring and the degree of correlation depends on the contribution of dust associated with each gas component in each ring to the total IR emission. A low degree of correlation can be the natural result of either a gas phase being less abundant (hence with a lower column density) or intrinsically less emissive with respect to other phases.

Two caveats of this approach have to be kept in mind:

(1) in the short IR bands (e.g. 8 μm), the emission is proportional to the product $N_{\rm H} \times G_0$, where $N_{\rm H}$ is the total hydrogen column density and G_0 represents a scaling of the Mathis, Mezger & Panagia (1983) radiation field in the solar neighbourhood (see e.g. Compiègne et al. 2010). This is also true at 24 μm and, partly, at 70 μm, given that these bands are contributed by emission from very small grains (VSGs) which, as polycyclic aromatic hydrocarbons (PAHs), are stochastically heated by the local radiation field. Conversely, the emission at wavelength longer than 70 μm is produced by big grains (BGs) which are in thermal equilibrium with the radiation field. The G_0 intensity defines the BG equilibrium temperature, while the total hydrogen column density determines the absolute level of the BG emission. Hence, if the radiation field (therefore the BG equilibrium temperature) varies smoothly across the region, the intensity variations in the FIR emission are dominated by the column density variations across the field (Compiègne et al. 2010). As a result, the net effect is an increasing degree of correlation going from shorter to longer wavelengths.

(2) A second limitation of the inversion approach lies in the fact that, in order to solve equation (1), the column densities associated with each gas phase for each LOS have to be accurately recovered. However, this might not occur, either when part of the gas in a given phase is not traceable by standard methods (i.e. warm H_2), or when a fraction of the gas along the LOS absorbs rather than emitting (i.e. the cold H I). In the first case, the morphology of the column density maps is artificially altered, leading to an 'excess' of IR emission and to a consequent lower degree of correlation between the column density maps and the input IR maps. In the second case, if the optically thick regions are in correspondence of strong IR emission features, the column density maps, estimated in the optically thin limit, and the IR maps will show an anticorrelation.

Such a correlation can be investigated in terms of Pearson's coefficients (e.g. Edwards 1976). Given two vectors X and Y, Pearson's coefficient ρ is defined as the ratio between the covariance $\mathrm{cov}(X, Y) = \sum_{i=1}^{n}(X_i - \bar{X})(Y_i - \bar{Y})$ and the product of their standard deviations σ_X and σ_Y

$$\rho(X, Y) = \frac{\mathrm{cov}(X, Y)}{\sigma_X \sigma_Y}, \tag{10}$$

ρ is defined in the range $|\rho| \leq 1$ and $\rho \simeq 1$ indicates strong correlation, while $\rho \simeq -1$ suggests a strong anticorrelation.

Table 1 provides a summary of our computed Pearson's coefficients (ρ). Fig. 4 shows two examples of correlation plots, obtained from comparison of the 500 μm emission with the molecular and atomic column densities. These plots correspond to the highest

Table 1. Pearson's correlation coefficients for the input IR maps and the column density maps for each gas phase and ring. In Ring 1 (which includes the Scutum–Crux Arm), there is a high degree of correlation between the IR maps – at all wavelengths – and the column density maps of H I, H_2 and H II. A lower degree of correlation, even a signature of anticorrelation, is instead revealed by Pearson's coefficients between the column densities in Rings 2–4 and the input IR maps.

	Pearson's coefficient									
Band	*Ring 1*			*Ring 2*			*Ring 3*			*Ring 4*
(μm)	(4.25–5.6 kpc)			(5.6–7.4 kpc)			(7.4–8.5 kpc)			(8.5–16.0 kpc)
gas phase	H I	H_2	H II	H I	H_2	H II	H I	H_2	H II	H I
8	0.51	0.74	0.82	0.38	0.52	0.41	−0.44	0.28	−0.01	−0.10
24	0.27	0.52	0.65	0.21	0.34	0.28	−0.44	0.14	−0.04	−0.06
70	0.11	0.51	0.67	0.19	0.31	0.40	−0.53	0.10	0.02	−0.02
160	0.42	0.79	0.86	0.39	0.55	0.53	−0.46	0.21	0.07	−0.08
250	0.47	0.85	0.87	0.45	0.61	0.56	−0.41	0.21	0.15	−0.04
350	0.48	0.86	0.87	0.47	0.62	0.57	−0.41	0.22	0.14	−0.06
500	0.50	0.86	0.86	0.48	0.62	0.56	−0.40	0.21	0.15	−0.05

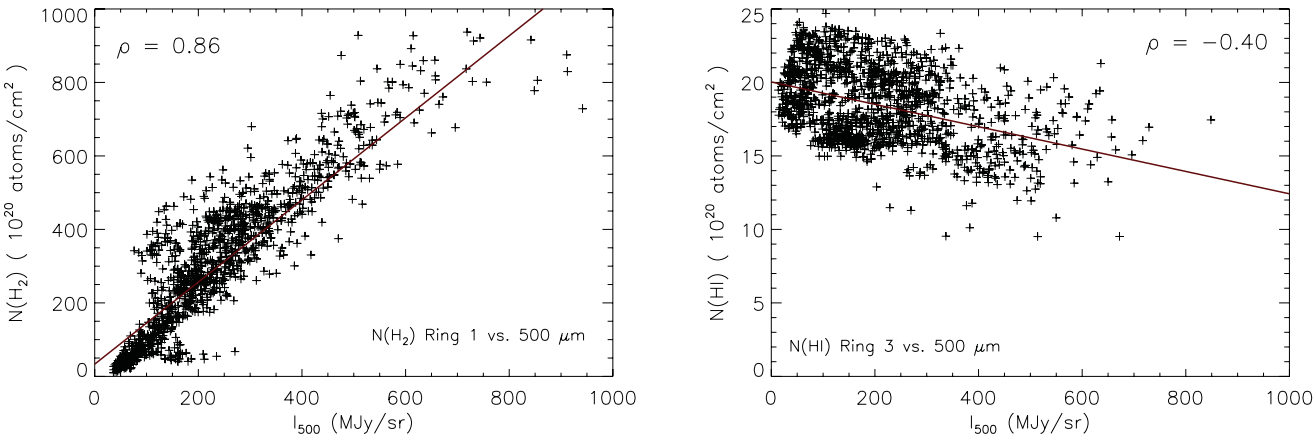

Figure 4. Correlation plots between Hi-GAL 500 μm map and $N(H_2)$ Ring 1 map (left-hand image) and Hi-GAL 500 μm map and N(H I) Ring 3 map (right). Pearson's coefficients are $\rho = 0.86$ and $\rho = -0.40$, respectively, the lowest and the highest between this IR map and the column density maps in this region.

($N(H_2)$, Ring 1) and lowest ($N(H\,I)$, Ring 3) degree of correlation among all the considered cases for the 500 μm emission.

The correlations in Ring 1 are the highest, at all wavelengths and for each gas phase. The correlation is significant (up to 0.87) for both the H_2 and H II column densities, while it is noticeably lower for the atomic phase. Averaging across wavelengths, we obtain: $\rho_{H\,I,Ring1} = 0.39$, $\rho_{H_2,Ring1} = 0.73$ and $\rho_{H\,II,Ring1} = 0.80$.

In general, the aromatic infrared bands (AIB, 8 μm and 24 μm) and the 70 μm band display a lower degree of correlation with respect to longer wavelengths, hence corroborating the hypothesis that they trace the intensity of the radiation field as well as the total hydrogen column density.

For Ring 2, we have that the average correlations are $\rho_{H\,I,Ring2} = 0.37$, $\rho_{H_2,Ring2} = 0.51$ and $\rho_{H\,II,Ring2} = 0.48$. These values are lower than for Ring 1, especially for H_2 and H II, indicating that Ring 2 either contributes less than the Scutum–Crux region to the total IR emission or that part of the gas is not entirely seen in emission with the standard tracers.

In Ring 3, the IR maps are poorly correlated with the molecular and ionized gas column densities and partially anticorrelated with the atomic gas column density. This is possibly due to the presence of gas not entirely traced by the standard tracers, as supported by observations of a cold layer of H I and strong individual absorption features located at 7.4 kpc $\leq R \leq$ 8.5 kpc (see Section 6.2).

A weak anticorrelation is also present in Ring 4. In this case, the negative Pearson's coefficients can be explained through a combination of both absorption features and intrinsic weak emission.

Pearson's coefficients also measure the correlation among the various gas phases in each ring. These coefficients are shown in Table 2. The correlation between atomic and molecular gas in Ring 1 is not very strong ($\rho_{H\,I,H_2,Ring1} = 0.34$), likely a consequence of the ubiquitous distribution of H I with respect to H_2. Conversely, molecular and ionized hydrogen appear to be strongly correlated ($\rho_{H_2,H\,II,Ring1} = 0.77$), as expected in star-forming regions. The correlation between H I and H II ($\rho_{H\,I,H\,II,Ring1} = 0.24$) likely reflects the fact that both phases have a diffuse component.

In Ring 2, Pearson's coefficients follow the same trend as in Ring 1, with a high correlation between molecular and ionized components ($\rho_{H_2,H\,II,Ring2} = 0.64$), confirming the tight spatial correlation among these two phases, and a partial correlation among H I and H II.

In Ring 3, there is evidence of anticorrelation between H I and H_2 components, indicating the presence of pixels with detected H_2 in correspondence of H I absorption features. In Section 6.2, we investigate the possible reasons behind this effect. The ionized gas in this region is dominated by the diffuse component, as there are no catalogued H II regions at 7.4 kpc $\leq R \leq$ 8.5 kpc towards this LOS, and it appears not to be associated with either H I nor H_2, as illustrated by the poor correlations (and, even, anticorrelation) with these phases.

Table 2. Pearson's coefficients for the correlation between different gas phases in each ring. In Rings 1 and 2, the molecular component is well correlated with the ionized component, while the atomic component, which is more ubiquitous, is less correlated with both H_2 and H II. The low/negative coefficients in Ring 3 are likely the consequence of an underestimate of the total column density.

	Pearson's coefficient		
Gas phases	*Ring 1* (4.25–5.6 kpc)	*Ring 2* (5.6–7.4 kpc)	*Ring 3* (7.4–8.5 kpc)
H I–H_2	0.34	0.61	− 0.21
H I–H II	0.24	0.38	0.14
H_2–H II	0.77	0.64	− 0.09

6 DISCUSSION AND RESULTS

In the following, we solve equation (1) to recover the emissivities for dust associated with the different gas phases in each ring. The code converges and retrieves positive and reliable emissivity coefficients only in Ring 1 (Section 6.1) which, as we show in Section 6.3 and Appendix B, dominates the IR emission at all wavelengths. For Rings 2, 3 and 4, where more than 50 per cent of Pearson's coefficients across all the wavelengths are lower than 0.5, the code either does not converge or returns negative emissivities (Section 6.2). Whereas these results are difficult to interpret at first, they take a more clear meaning when we investigate the presence of matter not entirely accounted for by the gas tracers (Sections 6.2 and 6.4). Finally, we analyse the consequences of excluding the ionized gas component from the decomposition, a procedure often adopted in past inversion works (Section 6.5).

6.1 Ring 1: fitting the emissivities with DustEM

The emissivities for dust associated with the different gas phases in Ring 1 are shown in Table 3. We fit these with the DustEM model (Compiègne et al. 2011) which incorporates three populations of dust grains: PAHs, hydrogenated small amorphous carbons (VSGs), and a combination of large amorphous carbons and amorphous silicates (BGs). The DustEM fits are shown in Fig. 5. We note that the dust properties in SDPF1 are evaluated with respect to a reference spectral energy distribution (SED) obtained for the diffuse ISM at high ($|b| > 15^\circ$) Galactic latitudes (hereafter referred to as DHGL).

From DustEM, we estimate the intensity of the radiation field associated with each phase of the gas. We obtain, for the ratio between the local radiation field and the Mathis et al. (1983) value for the solar neighbourhood, G_0: $G_0(H\,I) = 1.54 \pm 0.23$, $G_0(H_2) = 1.55 \pm 0.51$ and $G_0(H\,II) = 4.47 \pm 0.75$. In the ionized phase, the radiation field is remarkably higher than in the other phases and consistent with a star formation scenario.

Dust temperatures are evaluated by DustEM separately for each of the three gas phases by applying (Bernard et al. 2008)

$$T_d = 17.5 \times G_0^{1/(4+\beta)}, \quad (11)$$

with the spectral emissivity index $\beta = 1.9$, in agreement with the result of Paradis et al. (2010) for this field. We find $T_{d,H\,I} = 18.82 \pm 0.47$ K, $T_{d,\,H_2} = 18.84 \pm 1.06$ K and $T_{d,H\,II} = 22.56 \pm 0.64$ K. As expected, dust in the ionized gas phase is warmer compared to dust

Table 3. Emissivities, and corresponding uncertainties, of dust associated with the three gas phases in Ring 1.

Band (μm)	ϵ_ν [MJy sr^{-1} (10^{20} H atoms cm^{-2})$^{-1}$]		
	H I	H_2	H II
8	0.839 ± 0.073	0.033 ± 0.012	0.116 ± 0.018
24	0.380 ± 0.141	0.014 ± 0.010	0.101 ± 0.016
70	3.443 ± 0.629	0.400 ± 0.217	2.546 ± 0.401
160	13.387 ± 1.687	1.736 ± 0.463	5.743 ± 0.670
250	11.611 ± 1.308	1.470 ± 0.204	3.343 ± 0.235
350	4.922 ± 0.312	0.606 ± 0.092	1.168 ± 0.132
500	1.820 ± 0.162	0.249 ± 0.026	0.388 ± 0.058

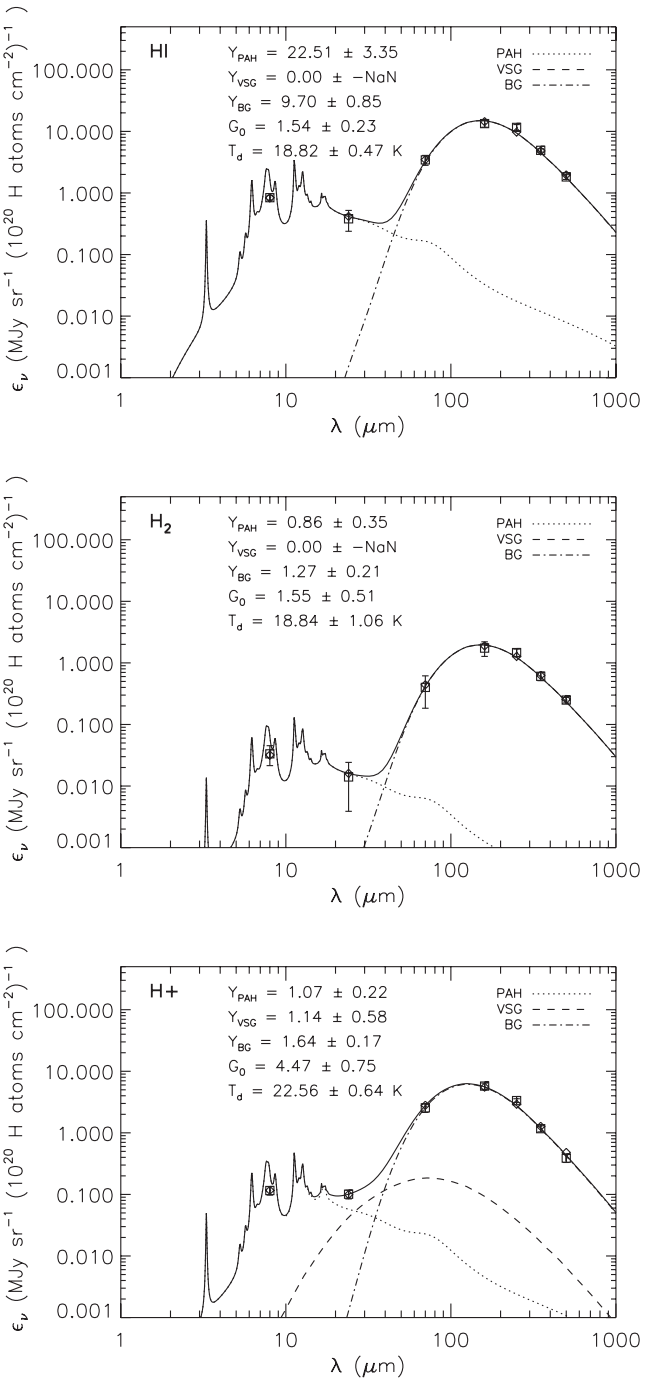

Figure 5. DustEM fit of the emissivities evaluated with the inversion model for dust associated with the H I (top panel), H_2 (medium panel) and H II (lower panel) gas components. The PAHs, VSGs and BGs contributions to each SED are plotted with dotted, dashed and dash–dotted line, respectively. G_0 and $Y_{\rm PAHs,\ VSGs,\ BGs}$ are defined in the text. The results are for Ring 1 only.

in the atomic and molecular phases since, in the proximity of star-forming complexes, the radiation causing ionization of interstellar hydrogen also induces heating of dust particles.

In DustEM, under the assumption of a constant gas-to-dust mass ratio in each gas phase, dust abundances are expressed relative to H atoms (Compiègne et al. 2010), $[M_{\rm PAH}/M_{\rm H}]$, $[M_{\rm VSG}/M_{\rm H}]$ and $[M_{\rm BG}/M_{\rm H}]$. In addition, the code retrieves abundances normalized to the values in the DHGL (Compiègne et al. 2010). We refer to these normalized abundances as $Y_{\rm PAH}$, $Y_{\rm VSG}$ and $Y_{\rm BG}$. From the fits of the emissivities in Ring 1, we obtain $Y_{\rm PAH}({\rm H\,I}) = 22.51 \pm 3.35$, $Y_{\rm PAH}(H_2) = 0.86 \pm 0.35$, $Y_{\rm PAH}({\rm H\,II}) = 1.07 \pm 0.22$ and $Y_{\rm BG}({\rm H\,I}) = 9.70 \pm 0.85$, $Y_{\rm BG}(H_2) = 1.27 \pm 0.21$, $Y_{\rm BG}({\rm H\,II}) = 1.64 \pm 0.17$. Surprisingly, both in the atomic and molecular phase, DustEM is able to reproduce the emissivity values without invoking a VSG contribution. Only in the ionized phase, we have $Y_{\rm VSG}$ different from zero and equal to $Y_{\rm VSG}({\rm H\,II}) = 1.14 \pm 0.58$. Noteworthy, the apparent lack of VSGs in the atomic and molecular gas phases could be ascribed to the limitation of the 3D-inversion model in accounting for the dependence of the AIB emission on the intensity of the radiation field, as discussed in the previous section. Furthermore, for very low values of $Y_{\rm BG}$, DustEM is not able to distinguish between a PAH and a VSG contribution, and typically tends to increase $Y_{\rm PAH}$ at the expense of $Y_{\rm VSG}$.

Most importantly, the result of the fit reveals a significant decrease of the relative abundance of PAHs in the molecular and ionized phase with respect to the neutral phase. In fact $[Y_{\rm PAH}({\rm H\,I})/Y_{\rm BG}({\rm H\,I})] = 2.3$, $[Y_{\rm PAH}(H_2)/Y_{\rm BG}(H_2)] = 0.67$ and $[Y_{\rm PAH}({\rm H\,II})/Y_{\rm BG}({\rm H\,II})] = 0.65$, suggesting that PAHs are somehow depleted in these two environments. The destruction of PAHs in the ionized gas has been investigated from a theoretical standpoint by Draine (2011) and observational evidence of these predictions are reported by e.g. Povich et al. (2007) and Paradis et al. (2011). For PAH depletion in the molecular gas component, although no theoretical prescription is readily available to interpret this result, we speculate, along the lines of Paradis et al. (2011), that this effect could be attributed to both the interstellar and local radiation field, i.e. by penetrating the cloud and causing partial destruction of the aromatic molecules.

6.2 Ring 2–3–4: missing column density and *dark gas*

In Rings 2, 3 and 4 ,the code either retrieves only partial positive solutions or does not converge. The emissivities and the associated errors for these rings are in Table 4. Although the results in the table do not have a direct physical interpretation (i.e. negative emissivities), they are an indication of the limitations of the basic assumptions of our model. From equation (1) and under the hypothesis of a single emissivity value for each gas component, the integrated IR emission is expected, by construction, to positively correlate with the gas column densities (see Section 5). In this framework, the negative emissivities obtained in Ring 2–3–4 suggest that in these regions the model fails to adequately reproduce the details of emission associated with each gas phase. In the following, we investigate whether the failure of the model can be attributed to a mismatch between the column densities retrieved by the tracers described in Section 4.3 and the actual total amount of gas located in these rings.

Grenier et al. (2005) have shown, by comparing H I/CO data with *gamma*-ray emission, the existence in the solar neighbourhood of the so-called *dark gas*, a mixture of cold H I, which is optically thick in the 21 cm line, and warm H_2 which cannot be observed with the standard tracers. They claim that, although it is not clear which component (cold H I or warm H_2) dominates, the contribution from dark H_2 must be considerable, up to 50 per cent of the total column density in regions where there is no CO detection. An important dark gas contribution to the overall IR emission is also reported in Planck Collaboration (2011a). In this inversion analysis, applied to

Table 4. Emissivities, and corresponding uncertainties, of dust associated with the three gas phases in Ring 2–3–4.

Band (μm)	ϵ_ν [MJy sr^{-1} (10^{20} H atoms cm^{-2})$^{-1}$]						
	H I			H_2		H II	
	Ring 2	*Ring 3*	*Ring 4*	*Ring 2*	*Ring 3*	*Ring 2*	*Ring 3*
8	0.038 ± 0.166	− 1.766 ± 0.507	0.035 ± 0.198	0.086 ± 0.059	0.076 ± 0.043	− 0.059 ± 0.090	− 0.366 ± 0.134
24	0.194 ± 0.112	− 0.945 ± 0.416	0.147 ± 0.157	− 0.003 ± 0.048	0.055 ± 0.057	0.013 ± 0.076	− 0.484 ± 0.156
70	2.219 ± 2.240	− 7.109 ± 2.517	− 3.600 ± 0.892	− 0.577 ± 0.326	1.686 ± 0.676	1.849 ± 0.343	0.439 ± 1.841
160	4.611 ± 7.196	− 14.980 ± 10.86	− 16.330 ± 2.316	2.189 ± 0.909	0.332 ± 2.241	3.318 ± 1.644	4.331 ± 5.278
250	2.374 ± 3.456	− 23.792 ± 6.040	− 6.929 ± 2.683	2.298 ± 0.624	− 3.470 ± 1.806	0.038 ± 1.276	3.154 ± 1.276
350	0.970 ± 1.409	− 6.615 ± 3.321	− 2.587 ± 0.604	0.698 ± 0.450	− 1.346 ± 0.746	0.202 ± 0.447	1.681 ± 0.739
500	0.198 ± 0.391	− 3.122 ± 1.627	− 0.555 ± 0.203	0.268 ± 0.174	− 0.570 ± 0.401	− 0.090 ± 0.153	0.701 ± 0.377

the entire Galactic plane at 1° resolution, the authors find that *dark gas* is mostly distributed around major molecular cloud complexes.

Theoretical predictions from Wolfire, Hollenbach & McKee (2010) indicate that a significant amount of warm H_2 is located in the exterior of photodissociation regions, where the transition of atomic into molecular gas occurs. Recent *Herschel*-HIFI CII observations by Pineda et al. (2013) have allowed us to slightly revise the early estimate by Grenier et al. (2005) relative to the total amount of dark H_2 in the Galaxy. These authors estimate that warm H_2 is likely to account for $\simeq$ 30 per cent of the total molecular gas, and find that the fraction of dark H_2 increases with Galactocentric distance. Therefore, with the standard CO tracers, we have an intrinsic limitation in estimating all the H_2 along the LOS.

In light of the considerations above, we have re-analysed the content of Ring 2–3–4 and checked if the negative emissivities derived for these rings can be due to the presence of untraced gas, specifically warm H_2 and cold H I. In Ring 2, we note (Fig. 3) that both CO isotopes are characterized by a pronounced peak of emission, indicating the presence of molecular clouds which, following the results from Planck Collaboration (2011c), might be associated with warm H_2. The same peak of emission in ^{12}CO and ^{13}CO is also observed in correspondence of Ring 3. However, in this case, as mentioned in Sections 2 and 4.3.1, a cold H I layer is also found, as reported by Gibson et al. (2004). The existence of cold (i.e. optically thick) H I could explain the anticorrelation and the lack of convergence of the code (Section 5). From the inspection of the VGPS data cube for SDPF1, we have identified two additional prominent features (either HISA or HICA) in the same range of Galactocentric radii:

(1) H30.74−0.05 at $11 \leq V_{\rm LSR} \leq 15$ km s^{-1},
(2) H30.39−0.24 at $8 \leq V_{\rm LSR} \leq 14.5$ km s^{-1}.

For these cold regions, we have made an attempt to derive an indicative upper limit of their spin temperatures by measuring the maximum of the median $T_{\rm b}$ values evaluated in the pixels in proximity of the regions of absorption. We recall that, as discussed in Section 4.3.1, the spin temperature of cold H I is noticeably lower than in the WNM, and that $T_{\rm s}$ is meaningful only in the case of warm H I in optically thin conditions. For this reason, it cannot be used to derive H I column densities in regions populated by different H I components (e.g. Strasser & Taylor 2004). Fig. 6 shows the brightness temperature profiles for the cold features H30.74−0.05 and H30.39−0.24, for which we obtain a mean value in each feature of $T_{\rm b} = 48.6$ and 38.7 K, respectively.

Interestingly, HISA features have been found mixed with molecular clouds. For instance, in the Perseus star-forming region, a significant fraction of cold H I is undergoing the transition to the molecular phase, and the HISA features appear to be non-gravitationally bound regions of molecular material not detected in CO (Klaassen et al. 2005).

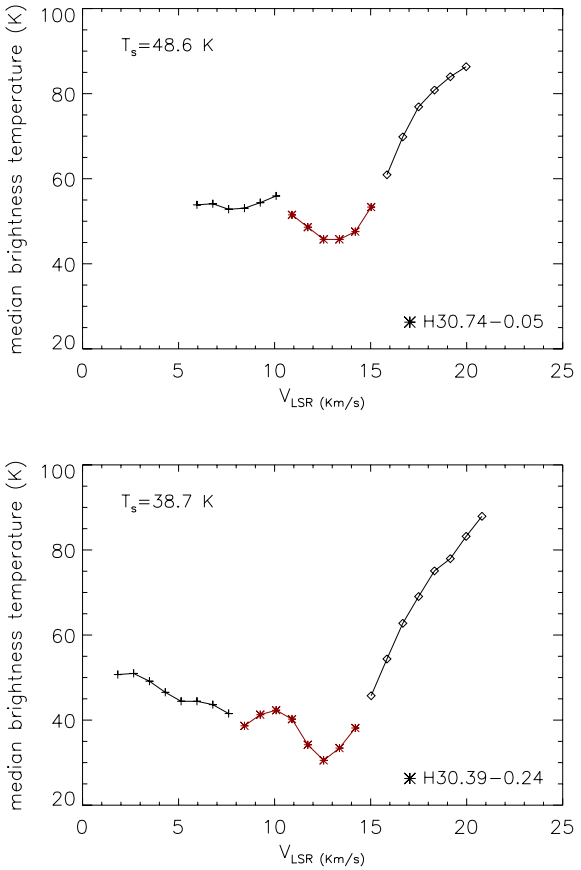

Figure 6. Maximum of the median brightness temperature (red line) in the surrounding of H30.74−0.05 and H30.39−0.24. Shown is the mean of these values across each feature. For comparison, the black line denotes the maximum of the median brightness temperatures measured in the same region at the nearby Galactocentric positions.

In summary, we speculate that in Ring 2 the derivation of dust emissivities possibly fails due to a significant amount of warm H_2 not properly accounted for by the ^{12}CO and ^{13}CO data, while in Ring 3 the lack of convergence could be ascribed to both (untraced) warm H_2 and (badly traced) cold H I. Regarding Ring 4, our current hypothesis is that, after subtracting the contributions from the other rings and given the small amount of H I (only a few per cent, see Section 4.3.4), the code has little to no leverage to return meaningful values.

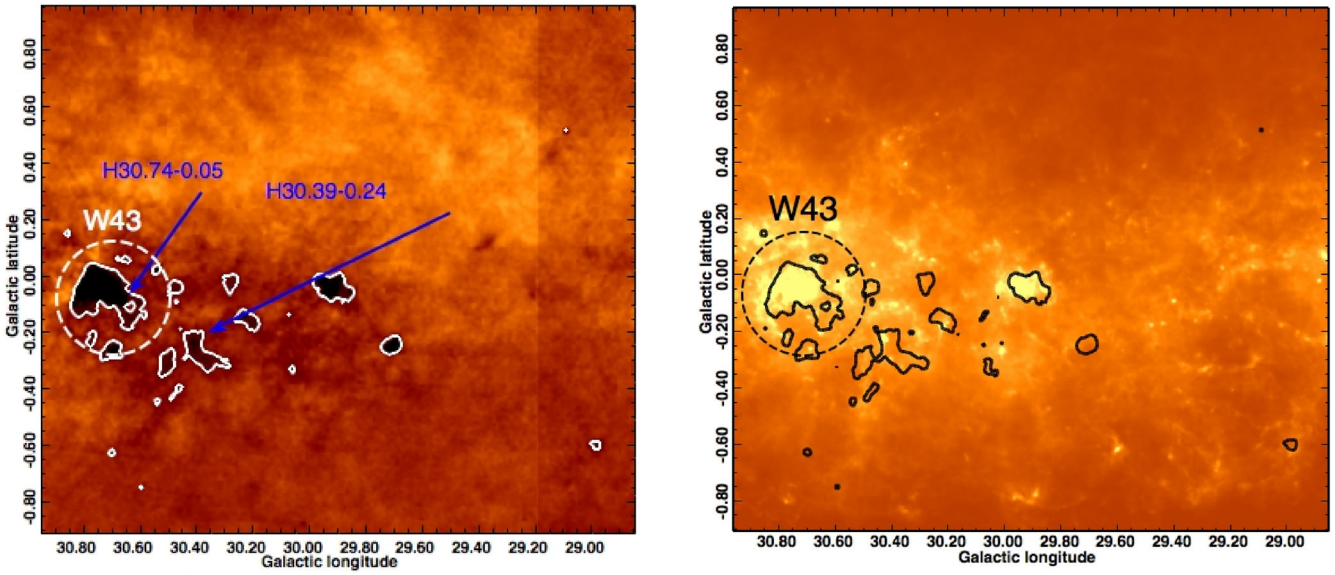

Figure 7. H I brightness temperature map integrated over Ring 3 (left-hand panel) and Hi-GAL 500 μm data (right-hand panel). The white contours in the H I map denote HICA and HISA features. The same regions at 500 μm (the black contours) overlap with either the W43 complex or with other H II regions in the field. In the H I map, some of the dark pixels within the cold features are pixels where T_b is negative due to strong absorption. The majority are found associated with the brightest H II regions, especially W43 and G29.944−0.04.

6.2.1 Solving for the distance ambiguity of cold H I features

As a by-product of our study, we can solve for the distance ambiguity of some of these cold features by comparing the H I data with the maps for the other tracers as well as with the input IR maps. In Fig. 7, we show the absorption features in silhouette against the warm background provided by the H II regions in SDPF1 compared to the VGPS 21-cm map integrated along Ring 3. H30.74−0.05 is dominated by absorption of the continuum background provided by W43, and it is therefore primarily an HICA feature. Since W43 is at the tangent point of the Scutum–Crux Arm, we can solve the distance ambiguity for this cold structure and locate it at $0.7 \leq d \leq 1.1$ kpc, i.e. on the Sagittarius–Carina Arm (see Fig. 1). In addition, the 29 H II regions in SDPF1 are distributed between Rings 1 and 2 (Anderson & Bania 2009), thus all the absorption features, including H30.39−0.24, observed in Ring 3 in correspondence of these H II regions are also likely associated with the Sagittarius–Carina Arm.

6.3 The dominant contribution of Ring 1 to the integrated intensity maps

In Section 4.3.4, we have seen that roughly 65 per cent of the total gas column density of SDPF1 is located in Ring 1. In this section, we want to show that dust emission associated with this ring accounts indeed for the bulk of dust emission in the input maps. To this end, we compare the longitude profiles of the output model with those of the input maps, and in doing so we consider the model contribution from Ring 1 only. The longitude intensity profiles are generated by averaging, for a given Galactic longitude, all latitude pixel values. These profiles, as well as the residuals obtained by subtracting the model from the input maps are shown in Fig. 8.

The model intensities obtained from Ring 1 appear to satisfactorily reproduce the input intensities at 24, 70 and 160 μm, with a discrepancy of less than 10 per cent. At longer wavelengths, the model tends to overestimates the input profiles and the discrepancy is more pronounced, of the order of 30 per cent. This effect is likely related to the fact that dust associated with the cold untraced gas, which would emit at long wavelengths (e.g. >160 μm), is mostly located outside Ring 1 (see Section 6.1). Therefore, its contribution is visibly missing when only Ring 1 is considered, and this produces the observed model overshooting. Conversely, in the range $24\,\mu\text{m} < \lambda < 160\,\mu\text{m}$ both dust and gas are properly accounted for and the model is able to reproduce the input emission. We note that at 8 μm the residuals are higher comparatively to other wavelengths and of the order of 40 per cent. This is expected: at this wavelength the coarse assumption of the model of a one-to-one correlation between input intensity and column densities reveals its limitation, due to the degenerate PAH emission dependence on both radiation field amplitude and column density (Section 5).

The residuals obtained from our analysis are comparable to earlier results. For instance, from the longitude profiles of Paladini et al. (2007), in the region of overlap with this work, i.e. $29^\circ < l < 31^\circ$, and between 60 and 240 μm, the residuals appear to be in the range 10–30 per cent. Planck Collaboration (2011c) provide residuals only at 1.4, 30 and 857 GHz (350 μm). No longitude profiles are given. At the common 350 μm wavelength and for $29^\circ < l < 31^\circ$, the residuals are of the order of 15–20 per cent. Considering that both Paladini et al. (2007) and Planck Collaboration (2011c) work on the full sky at a 1° resolution, the residuals obtained for our 2×2 square degree decomposition at 14.8 arcmin are in excellent agreement with these previous analyses.

In summary, the test shows that Ring 1 accounts for approximately 70–90 per cent of the total emission in the input maps at all wavelengths, while the combined Rings 2, 3 and 4 contributes only for the remaining 30–10 per cent, therefore strongly corroborating our earlier statement that, despite the lack of meaningful convergence of the method in the other rings, the results of Ring 1 are robust. In Appendix B, we will return on this point, by further investigating possible biases introduced by Rings 2, 3 and 4.

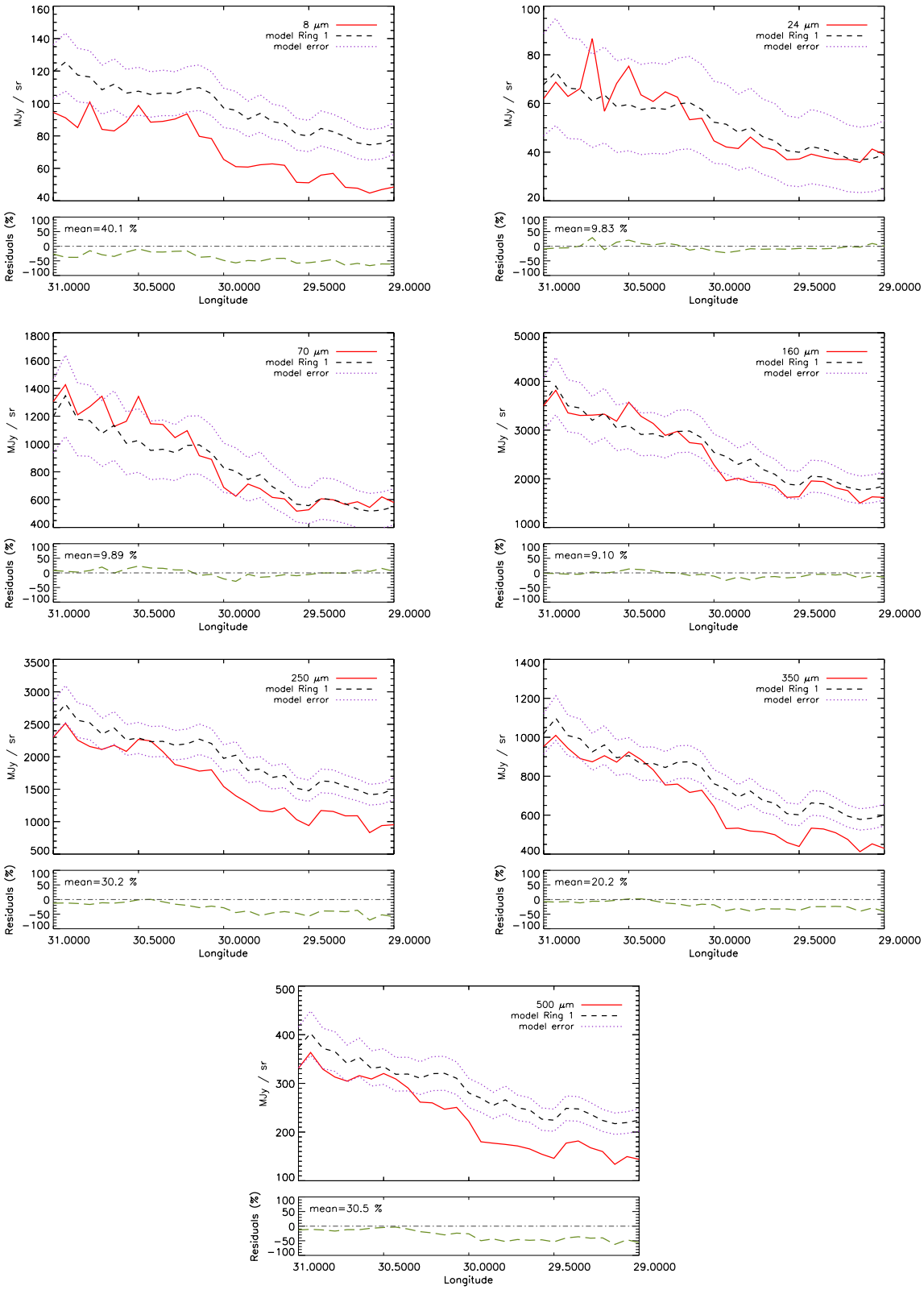

Figure 8. Comparison of the intensity longitude profiles for the input maps (red line) and for the Ring 1 inversion model (black dotted line). Overlaid are the $\pm 1\sigma$ boostrap errors (magenta dotted line). The separate panels at the bottom of the longitude profiles show the residuals (in percentage) obtained by subtracting the inversion model for Ring 1 from the input profiles (dashed green line).

6.4 Total column density and extinction maps

An alternative method to recover the missing hydrogen column density is through extinction. We have attempted to generate an extinction map for SDPF1 using colour excess templates derived from observations of giant stars. For this purpose, we use UKIDSS (Lawrence et al. 2007) and 2MASS (Skrutskie et al. 2006) JHK_s and GLIMPSE (Churchwell et al. 2009) 3.6 and 4.5 μm data. The first step is to minimize contamination from sources other than giants, in particular from dwarf stars. To this end, we first build colour–magnitude $J-K_s/K_s$ and $J-[3.6]/[3.6]$) diagrams using the photometric measurements provided in the UKIDSS/2MASS/GLIMPSE catalogues. Then, we compare these with the predictions from the Besançon Stellar Population Synthesis Model (Robin et al. 2003). From this model, we derive the colour criteria to separate the dwarf from the giant stars, i.e. $K_s \geq (J-K_s) \times 3.8 - 7.8$ and $[3.6] \geq (J-[3.6]) \times 3.2 + 7.4$ (see Fig. 9). Applying these criteria, we select 45 per cent of the sources in the original catalogues, in practice 4.4×10^5 out of $\simeq 10^6$ sources. The colour excess in H and K_s bands measured for the selected sources is converted into extinction using the extinction law derived by Rieke & Lebofsky (1985). At longer wavelengths, the correct extinction law is still a matter of debate. Variations have been reported to occur from one molecular cloud to another, and even within the same cloud (Cambrésy et al. 2011, and references therein). Also, the extinction law appears to change with Galactocentric radius (Zasowski et al. 2009). For this work, we adopt the extinction law derived by Cambrésy et al. (2011) in the Trifid Nebula. The extinction law values are: $A_{K_s}/A_V = 0.112$, $A_H/A_{K_s} = 1.56$, $A_{[3.6]}/A_{K_s} = 0.611$ and $A_{[4.5]}/A_{K_s} = 0.500$. The resulting A_V map is a combination of two maps: for visual extinctions <10 mag, it is generated using H and K_s bands, while for $A_V > 15$ mag it is obtained using the 3.6 and 4.5 μm bands. In the range $10 \leq A_V \leq 15$ mag, it is a linear combination of the two. The zero-point ($A_V = 6$ mag) is evaluated from the 2MASS data for $|l| \leq 10°$.

The final extinction map, with a resolution of 1 arcmin, is shown in Fig. 10. This map is converted into total hydrogen column density using the relation (Güver & Özel 2009)

$$N(\mathrm{H\,I}) = 22.1\ A_V \qquad [10^{20}\ \mathrm{atoms\,cm^{-2}}]. \tag{12}$$

We then compare the total column density map derived from extinction with the one derived from the gas tracers, obtained by summing up the individual contributions from the three gas phases and from each ring (see Fig. 11). From this comparison, we find that the extinction column density map, minus an offset of roughly 100×10^{20} atoms cm^{-2}, is lower with respect to its gas tracers counterpart by ∼70 per cent. We formulate the hypothesis that this discrepancy is mainly due to the fact that the gas tracers allow us to probe much larger distances with respect to the catalogued giants. To verify this scenario, we first note that Fig. 3 shows that the bulk of material in SDPF1 is within $R < 8.5$ kpc, corresponding for this LOS to 14.7 kpc, at the far distance. Therefore, the extinction map has to reach at least this distance in order to compare in column density with the gas tracers. Although we do not have an individual distance estimate for all our giants, we can use the Besançon model to have a rough idea of their distance distribution. Fig. 12 illustrates the number of sources as a function of solar distance for the selected giants and dwarfs. Most of the sources appear to be located around 10 kpc, setting the approximate limit of our extinction map and showing that, at least with the available data, extinction is not yet a viable route for estimating accurate column densities towards the inner Galaxy.

We have also explored an alternative approach, based on the model of Marshall et al. (2006), which allows building extinction maps in 3D. This model makes use of the combined 2MASS Point Source Catalog and Besançon model to calculate the extinction at increasing solar distances. The maximum distance reached towards any given LOS depends on the completeness in J and K_s bands in the 2MASS catalogue as well as on the effective column density. After generating an extinction map for SDPF1 following this prescription, we have compared the corresponding column density map with the one derived from the gas tracers. The comparison is not straightforward. In fact, although the Marshall et al. (2006) extinction map has a resolution of 15 arcmin, which is comparable to our working resolution (14.8 arcmin), the data are not Nyquist sampled, as the pixel size is also set to 15 arcmin. Therefore, for consistency the spatial resolution of the gas tracers' column density map is also downgraded to 15 arcmin using a 15 arcmin pixel size. With this procedure, we obtain a total of 50 pixels in each map.

The analysis is limited to the Galactocentric ring containing the Scutum–Crux Arm intersection, which is the only region accurately reconstructed by the Marshall et al. (2006) model. Fig. 13 shows the comparison of the column density estimated from the Marshall et al. (2006) extinction map with the column density evaluated from the tracers of the gas phases. We notice, as for Fig. 11, that the two column density maps are separated by an offset which, in this case, is of the order of $\simeq 500 \times 10^{20}$ atoms cm^{-2}. Moreover, the column densities computed from the 3D extinction map are even lower than those obtained from the previous extinction map, accounting only for ∼9 per cent of the gas column densities.

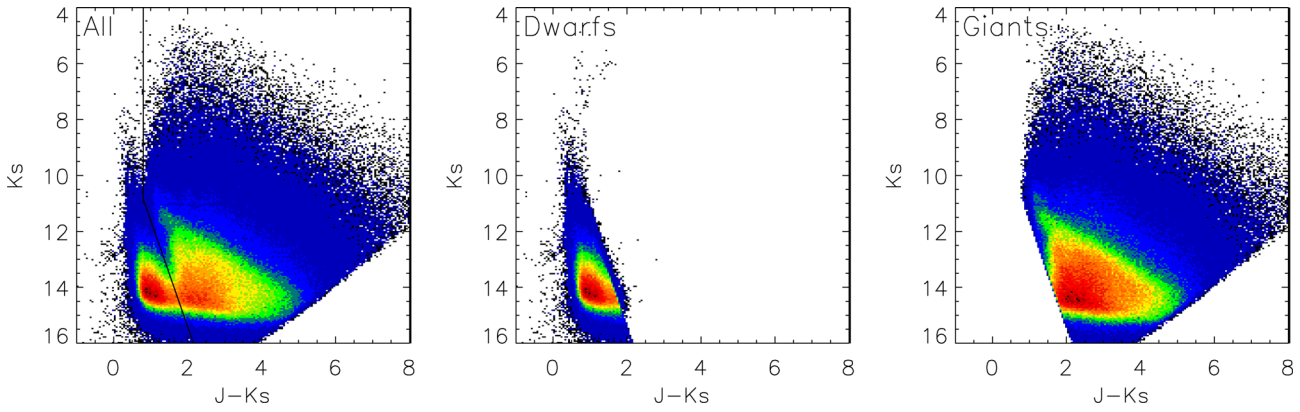

Figure 9. K_s versus $J-K_s$ diagrams. The black line in the left-hand panel corresponds to the cut applied to remove from the sample contaminating dwarfs. Identified dwarfs and giants are shown in the middle and right panel, respectively.

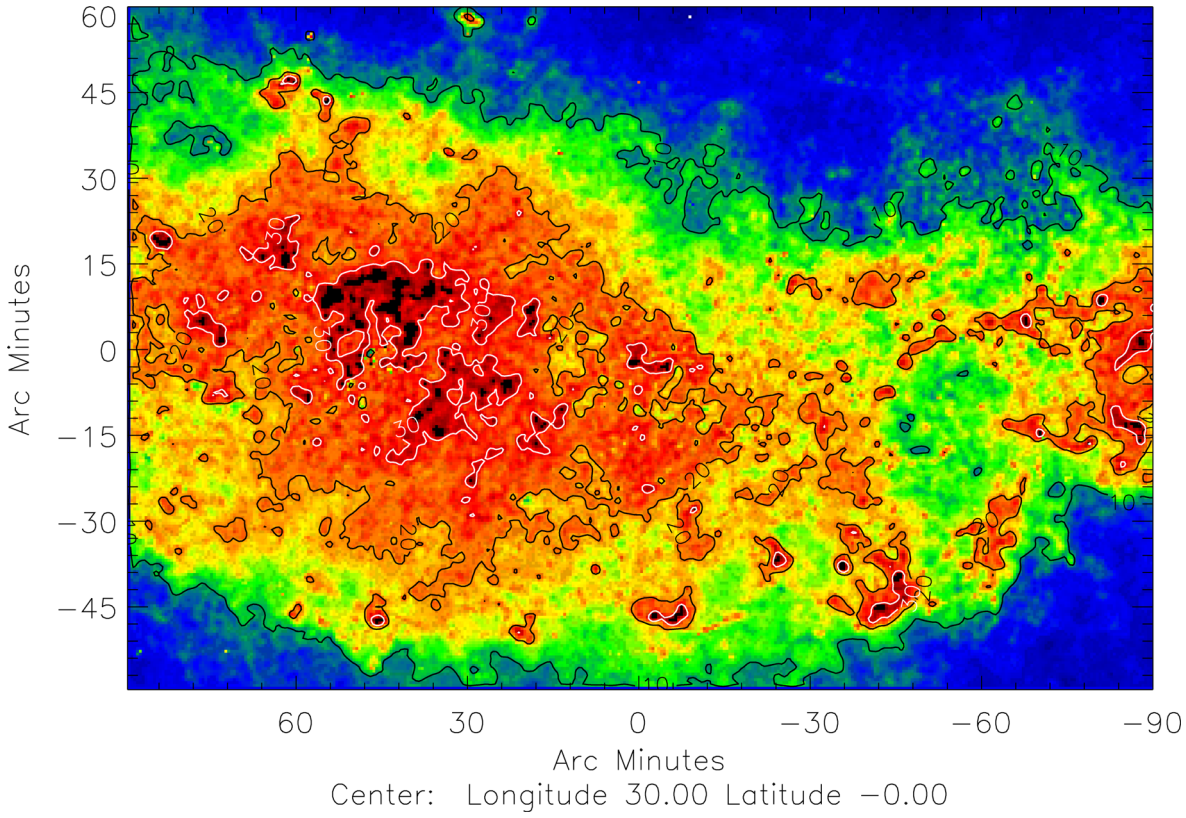

Figure 10. Extinction map obtained from giant stars in the UKIDSS, 2MASS and GLIMPSE catalogues. The resolution is 1 arcmin. Units are magnitude of A_V. The contours correspond to A_V of 10, 20 and 30 mag. Regions with the highest extinction (dark red) are associated with cold H I features.

6.5 Testing the exclusion of the ionized phase from the inversion model

Pearson's coefficients study described in Section 5 show the existence, at every wavelength, of a high degree of correlation between the ionized gas column density and IR emission, in particular in Ring 1.

In this section, we explore the consequences of performing inversion analysis without taking into account the ionized gas phase. For this purpose, we carry out a simple test, consisting in deriving the emissivity coefficients for Ring 1 ignoring the RRL data. We note that, if we do not make use of these data, we can afford to work at a higher resolution, hence with a larger number of pixels. By including only the atomic and molecular gas components, the pixel size is set by the ^{12}CO data, i.e. 3 arcmin, and we obtain ∼1200 pixels in each map, almost twice the previous number.

We now solve equation (1) [setting $N(\mathrm{H\,II}) = 0$ in all rings and pixels] and analyse the recovered emissivities, focusing on the long wavelengths (>70 μm), which we can model with a simple grey-body. The fitted SEDs for both the atomic and molecular phases are shown in Fig. 14. We fix the grey-body spectral emissivity index to $\beta = 1.9$ to be consistent with the results obtained including also the RRLs in the analysis (see Section 6.1). From the fit, we obtain $T_{\mathrm{d,H\,I}} = 19.81 \pm 0.70$ K and $T_{\mathrm{d,H_2}} = 22.11 \pm 0.21$ K. We note that the temperature of dust in the molecular phase is now higher compared to what we obtained in Section 6.1, and comparable to our previous result for H I. This result can be explained once again in light of Pearson's coefficients displayed in Table 1: the correlation analysis shows that the second most correlated component, after the ionized gas, with the IR templates at all wavelengths, is the molecular gas phase. This, mathematically, translates into artificially boosted emissivities for dust associated with H_2, as the molecular phase compensates for the absence of the H II component.

7 CONCLUSIONS

We have investigated dust properties in a 2 × 2 square degree Hi-GAL field (SDPF1) centred on $(l,b) = (30^\circ, 0^\circ)$, in the wavelength range $8 \leq \lambda \leq 500$ μm. For this purpose, we have used an inversion technique, first introduced by Bloemen et al. (1986), to decompose the observed integrated IR emission into individual contributions associated with dust in the atomic, molecular and ionized phase of the gas and located at different Galactocentric distances. We have used, for the first time in an inversion analysis, RRLs to trace the ionized gas. In addition, the decomposition into Galactocentric bins (or *rings*) is performed exploiting the natural boundaries of the structures (i.e. segments of spiral arms) as they appear in the gas data cubes.

We have solved the inversion equation for all the decomposition rings (i.e. Rings 1, 2, 3 and 4), and obtained positive solutions only for Ring 1. A Pearson's coefficient and longitude profiles analyses reveal that Ring 1, which covers Galactocentric distances between 4.2 and 5.6 kpc and hosts the mini-starburst W43, dominates the total IR emission towards SDPF1. For this ring only, we have fitted with DustEM the emissivities retrieved by the inversion method. These fits allow estimating, for each phase of the gas, dust temperatures and abundances, as well as the intensity of the local radiation field normalized to the intensity of the radiation field in the solar neighbourhood. In particular we find, for the ionized gas phase with respect to the other gas phases,

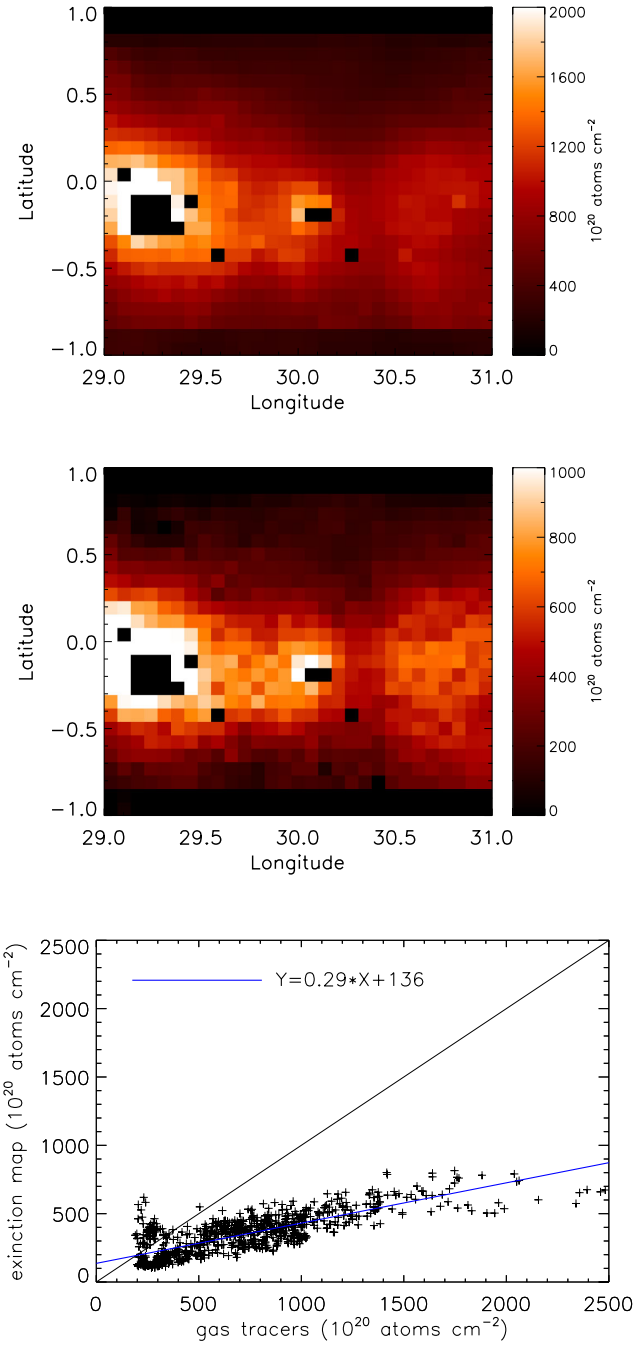

Figure 11. Top panel: column density map obtained by summing up the contributions of the three gas phases in each ring. Middle panel: column density map derived from the extinction map generated using giant stars. Both maps are convolved to 14.8 arcmin. Bottom panel: pixel-to-pixel correlation plot of the two column density maps. The blue line shows the best fit to the distribution. The black dot–dashed line denotes the $y = x$ relation.

an indication of PAH depletion and an intensity of the local radiation field two times higher, which reflects into a higher dust temperature.

For the other rings (Rings 2, 3 and 4), the inversion equation either cannot be solved or returns negative emissivities. Pearson's coefficients suggest a weak degree of correlation with the IR templates and, in a few cases, even an anticorrelation. For Rings 2

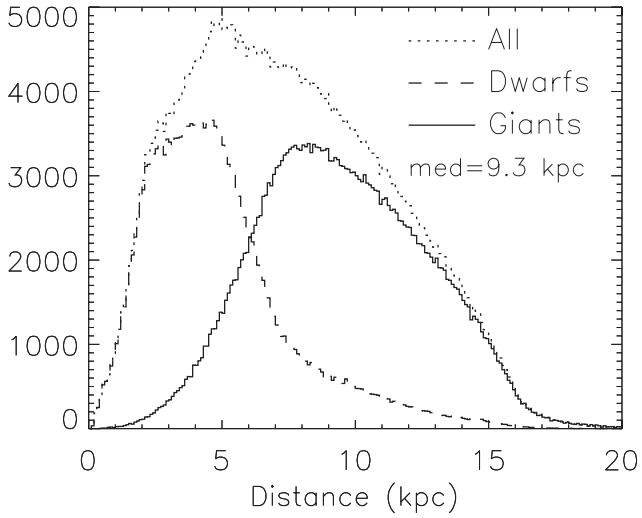

Figure 12. Number of sources as a function of solar distance for both the selected giant stars and the dwarfs from the Besançon model.

and 3, this result might be ascribed to the presence of a large amount of *untraced gas*, either associated with warm H_2 and/or cold H I. This hypothesis could find support in the fact that, in Ring 3, cold H I structures are indeed found. In this scenario, the column densities derived from the standard tracers would not be able to fully account for the observed IR emission; hence, the assumption of the inversion model would break down and the resulting emissivities (e.g. negative) be unreliable. In Ring 4, which covers the outer Galaxy, the slight degree of anticorrelation with the input IR maps is probably indicative of the intrinsic low emissivity of the region, due to a combined drastic decrease of both hydrogen column density and intensity of the interstellar radiation field.

We have investigated the role of extinction in evaluating total column densities along the LOS as an alternative method to gas tracers. For this purpose, we have attempted to build an extinction map for SDPF1 in two independent ways, i.e. using deep catalogues of giant stars and with a 3D-extinction model. Although both methods appear to be promising, they currently face the severe limitation of not being able to trace extinction beyond ∼10–15 kpc from the Sun.

Finally, we have explored the impact of neglecting the ionized gas phase in inversion analysis, as often done in the past. We have shown that, by not including this gas component, the temperature of dust associated with the molecular phase is artificially increased, due to its high degree of correlation with the input IR templates.

We conclude with a general remark. In this work, we have improved, with respect to previous inversion studies, the estimation of the H I, H_2 and H II column densities. However, we believe that this analysis has shown, above all, that local effects, such as departures from circular motion and the presence of cold H I structures (and, likely, warm H_2), become important when a 3D-inversion is performed in small sections of the plane and with an angular resolution higher than or comparable to the angular scale on which these effects dominate the total emission. Conversely, when the entire Galactic plane is *inverted* at low-angular resolution, the peculiarities of each LOS are averaged out. Further developments of 3D-inversion models will have to take into account these

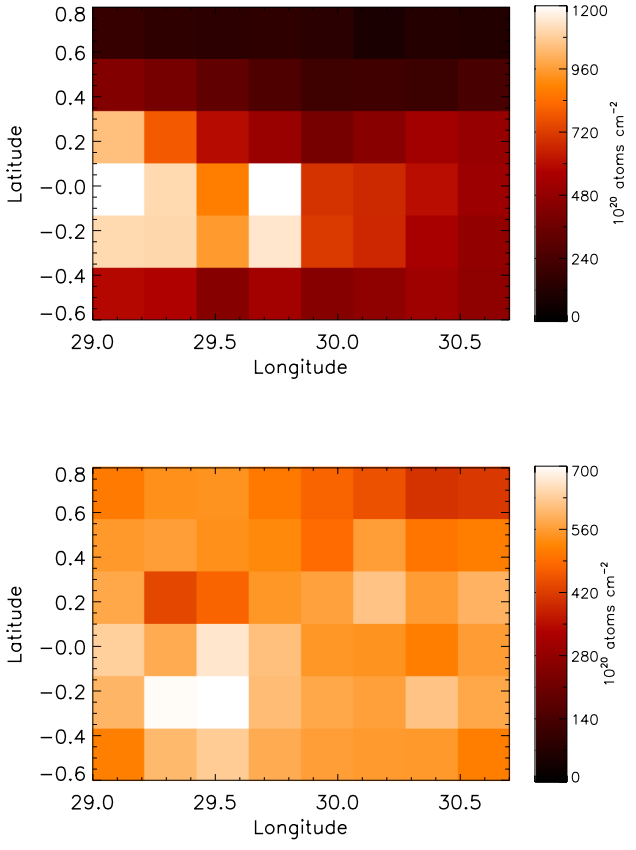

Figure 13. Same as Fig. 11 but for the extinction map obtained from the Marshall et al. (2006) model (middle panel). Both the column density map from the gas tracers (top panel) and the extinction map are downgraded to 15 arcmin, using a pixel size of 15 arcmin.

limitations, both by including non-radial motions, i.e. the grand spiral design of the Galaxy, and by estimating total column densities accounting for the blending of cold and warm material along the LOS.

ACKNOWLEDGEMENTS

The authors want to thank Mark Calabretta and Lister Staveley-Smith for their work on the RRL data. AT is supported by an STFC grant to JBCA. CD acknowledges an STFC Advanced Fellowship and an EU Marie-Curie grant under the FP7. MIRA acknowledges the support by the European Research Council grant MISTIC (ERC-267934). *Herschel* is an ESA space observatory with science instruments provided by European-led Principal Investigator consortia and with important participation from NASA.

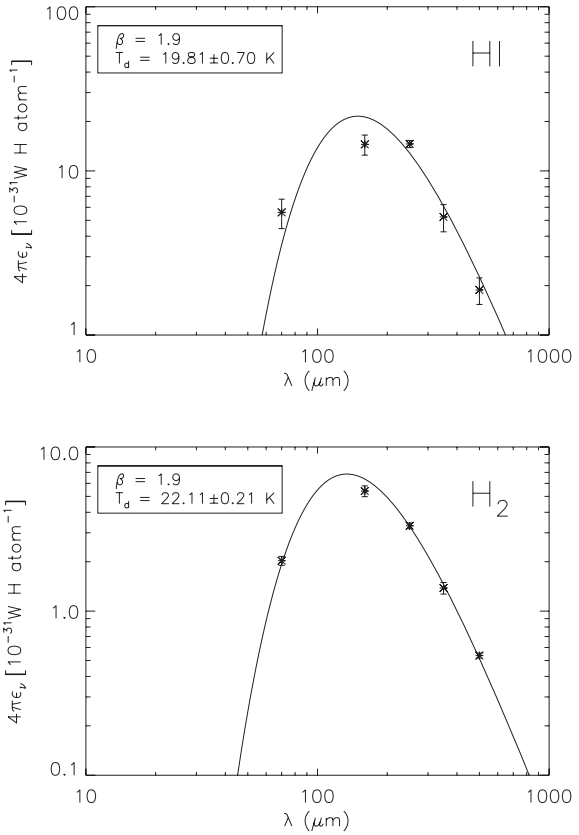

Figure 14. Grey-body fits to the dust emissivities associated with the atomic (top panel) and molecular (bottom) gas phases. Results refer to Ring 1 when the ionized gas component (i.e. the RRL data) is not included in the inversion equation.

REFERENCES

Abdo A. A. et al., 2010, ApJ, 710, 133
Alves M. I. R., Davies R. D., Dickinson C., Davis R. J., Auld R. R., Calabretta M., Staveley-Smith L., 2010, MNRAS, 405, 1654
Alves M. I. R., Davies R. D., Dickinson C., Calabretta M., Davis R., Staveley-Smith L., 2012, MNRAS, 422, 2429
Anderson L. D., Bania T. M., 2009, ApJ, 690, 706
Bally J. et al., 2010, A&A, 518, L90
Battersby C. et al., 2011, A&A, 535, A128
Benjamin R. A. et al., 2003, PASP, 115, 953
Bernard J.-P. et al., 2008, AJ, 136, 919
Bernard J. et al., 2010, A&A, 518, L88
Bloemen J. B. G. M. et al., 1986, A&A, 154, 25
Bloemen J. B. G. M., Deul E. R., Thaddeus P., 1990, A&A, 233, 437
Bolatto A. D., Wolfire M., Leroy A. K., 2013, ARA&A, 51, 207
Boulanger F., Perault M., 1988, ApJ, 330, 964
Boulanger F., Abergel A., Bernard J. P., Burton W. B., Desert F.-X., Hartmann D., Lagache G., Puget J.-L., 1996, A&A, 312, 256
Cambrésy L., Rho J., Marshall D. J., Reach W. T., 2011, A&A, 527, A141
Carey S. J. et al., 2009, PASP, 121, 76
Churchwell E. et al., 2009, PASP, 121, 213
Combes F., 1991, ARA&A, 29, 195

Compiègne M., Flagey N., Noriega-Crespo A., Martin P. G., Bernard J.-P., Paladini R., Molinari S., 2010, ApJ, 724, L44
Compiègne M. et al., 2011, A&A, 525, A103
Dickey J. M., Lockman F. J., 1990, ARA&A, 28, 215
Dickinson C., Davies R. D., Davis R. J., 2003, MNRAS, 341, 369
Diolaiti E., Bendinelli O., Bonaccini D., Close L., Currie D., Parmeggiani G., 2000, A&A, 147, 335
Draine B. T., 2011, ApJ, 732, 100
Dunham M. K., Rosolowsky E., Evans N. J., II, Cyganowski C., Urquhart J. S., 2011, ApJ, 741, 110
Duval J. R. et al., 2010, ApJ, 723, 492
Edwards A., 1976, The Correlation Coefficient. Freeman & Co., San Francisco
Efron B., 1979, Ann. Stat., 7, 1
Ferrière K. M., 2001, Rev. Mod. Phys., 73, 1031
Fich M., Blitz L., Stark A. A., 1989, ApJ, 342, 272
Giard M., Lamarre J. M., Pajot F., Serra G., 1994, A&A, 286, 203
Gibson S. J., 2010, in Kothes R., Landecker T. L., Willis A. G., eds, ASP Conf. Ser. Vol. 438, Cold Atomic Gas in the CGPS and Beyond. Astron. Soc. Pac., San Francisco, p. 111
Gibson S. J., Taylor A. R., Stil J. M., Higgs L. A., Dewdney P. E., Brunt C. M., 2004, in Alfaro E. J., Pérez E., Franco J., eds, Astrophysics and Space Science Library, Vol. 315, How Does the Galaxy Work? A Galactic Tertulia with Don Cox and Ron Reynolds. Kluwer, Dordrecht, p. 47
Gibson S. J., Taylor A. R., Higgs L. A., Brunt C. M., Dewdney P. E., 2005, ApJ, 626, 195
Grenier I. A., Casandjian J.-M., Terrier R., 2005, Science, 307, 1292
Griffin M. J. et al., 2010, A&A, 518, L3
Güver T., Özel F., 2009, MNRAS, 400, 2050
Haffner L. M. et al., 2009, Rev. of Mod. Phys., 81, 969
Haynes R. F., Caswell J. L., Simons L. W. J., 1978, Aust. J. Phys. Astrophys. Suppl., 45, 1
Heiles C., Troland T. H., 2003, ApJ, 586, 1067
Jackson J. M. et al., 2006, ApJS, 163, 145
Johannesson G., Moskalenko I., Digel S., 2010, preprint (arXiv:e-prints)
Klaassen P. D., Plume R., Gibson S. J., Taylor A. R., Brunt C. M. for the Fermi LAT Collaboration, 2005, ApJ, 631, 1001
Lagache G., Haffner L. M., Reynolds R. J., Tufte S. L., 2000, A&A, 354, 247
Lawrence A. et al., 2007, MNRAS, 379, 1599
Makovoz D., Marleau F. R., 2005, PASP, 117, 1113
Marshall D. J., Robin A. C., Reylé C., Schultheis M., Picaud S., 2006, A&A, 453, 635
Mathis J. S., Mezger P. G., Panagia N., 1983, A&A, 128, 212
Mezger P. G., Henderson A. P., 1967, ApJ, 147, 471
Molinari S. et al., 2010, PASP, 122, 314
Paladini R., Davies R. D., De Zotti G., 2004, MNRAS, 347, 237
Paladini R., De Zotti G., Davies R. D., Giard M., 2005, MNRAS, 360, 1545
Paladini R., Montier L., Giard M., Bernard J. P., Dame T. M., Ito S., Macias-Perez J. F., 2007, A&A, 465, 839
Paladini R. et al., 2012, ApJ, 760, 149
Paradis D., Veneziani M., Noriega-Crespo A., Lagache G., Kawamura A., Onishi T., Fukui Y., 2010, A&A, 520, L8
Paradis D., Paladini R., Noriega-Crespo A., Lagache G., Kawamura A., Onishi T., Fukui Y., 2011, ApJ, 735, 6
Peretto N., Fuller G. A., 2009, A&A, 505, 405
Pineda J. E., Caselli P., Goodman A. A., 2008, ApJ, 679, 481
Pineda J. L., Goldsmith P. F., Chapman N., Snell R. L., Li D., Cambrésy L., Brunt C., 2010, ApJ, 721, 686
Pineda J. L., Langer W. D., Velusamy T., Goldsmith P. F., 2013, A&A, 554, A103
Planck Collaboration 2011a, A&A, 536, A19
Planck Collaboration 2011b, A&A, 536, A20
Planck Collaboration 2011c, A&A, 536, A21
Planck Collaboration 2011d, A&A, 536, A22
Planck Collaboration 2011e, A&A, 536, A23
Planck Collaboration 2011f, A&A, 536, A24
Planck Collaboration 2011g, A&A, 536, A25
Poglitsch A. et al., 2010, A&A, 518, L2
Povich M. S. et al., 2007, ApJ, 660, 346
Quireza C., Rood R. T., Bania T. M., Balser D. S., Maciel W. J., 2006, ApJ, 653, 1226
Rathborne J. M., Johnson A. M., Jackson J. M., Shah R. Y., Simon R., 2009, ApJS, 182, 131
Rieke G. H., Lebofsky M. J., 1985, ApJ, 288, 618
Robin A. C., Reylé C., Derrière S., Picaud S., 2003, A&A, 409, 523
Russeil D., 2003, A&A, 397, 133
Sanders D. B., Clemens D. P., Scoville N. Z., Solomon P. M., 1986, ApJS, 60, 1
Shaver P. A., McGee R. X., Newton L. M., Danks A. C., Pottasch S. R., 1983, MNRAS, 204, 53
Skrutskie M. F. et al., 2006, ApJ, 131, 1163
Smith L. F., Biermann P., Mezger P. G., 1978, A&A, 66, 65
Sodroski T. J., Odegard N., Arendt R. G., Dwek E., Weiland J. L., Hauser M. G., Kelsall T., 1997, ApJ, 480, 173
Stahler S. W., Palla F., eds, 2005, The Formation of Stars. Wiley, New York
Staveley-Smith L. et al., 1996, PASA, 13, 243
Stil J. M. et al., 2006, ApJ, 132, 1158
Strasser S., Taylor A. R., 2004, ApJ, 603, 560
Strong A. W., Moskalenko I. V., Reimer O., Digel S., Diehl R., 2004, A&A, 422, L47
Tibbs C. T. et al., 2012, ApJ, 754, 94
Traficante A. et al., 2011, MNRAS, 416, 2932
Weaver H., Williams D. R. W., 1974, A&AS, 17, 251
Wilson T. L., Mezger P. G., Gardner F. F., Milne D. K., 1970, A&A, 6, 364
Wolfire M. G., Hollenbach D., McKee C. F., 2010, ApJ, 716, 1191
Zasowski G. et al., 2009, ApJ, 707, 510
Zavagno A. et al., 2010, A&A, 518, L101

APPENDIX A: DERIVING THE ^{13}CO COLUMN DENSITY USING BOTH ^{12}CO AND ^{13}CO DATA

Along each position (l,b) in the sky, the ^{13}CO column density is (Duval et al. 2010)

$$\frac{N(^{13}\mathrm{CO})(l,b)}{\mathrm{cm}^{-2}} = 2.6\times10^{14}\int \frac{T_{\mathrm{ex}}(l,b,v)\tau_{13}(l,b,v)}{1-\mathrm{e}^{\frac{-5.3}{T_{\mathrm{ex}}(l,b,v)}}}\frac{\mathrm{d}v}{\mathrm{km\ s^{-1}}}, \tag{A1}$$

integrated over the V_{LSR} range corresponding to each ring. Both T_{ex} and τ_{13} can be obtained starting from the detection equation (Stahler & Palla 2005):

$$T_{\mathrm{B}_0} = T_0[f(T_{\mathrm{ex}}) - f(T_{\mathrm{bg}})][1-\mathrm{e}^{-\tau_0}]. \tag{A2}$$

Here, T_{B_0} is the brightness temperature of each pixel at a given frequency which is related to the observed antenna temperature through the beam efficiency and beam dilution corrections. τ_0 is the optical thickness in the same position. Assuming the radiation behind the clouds is due only to the cosmic microwave background, $T_{\mathrm{bg}} = 2.7\,\mathrm{K}$. T_0 is the equivalent temperature of the transition: $T_0 = h\nu_0/K_B$. The function $f(T)$ is

$$f(T) = [\exp(T_0/T)-1]^{-1}. \tag{A3}$$

Inverting equation (A2) and fixing $T_0 = 5.29\,\mathrm{K}$ for the ^{13}CO $J = 1 \rightarrow 0$ transition (Pineda et al. 2010), one can obtain the expression for the ^{13}CO optical depth at each position (Duval et al. 2010):

$$\tau^{13}(l,b,v) = -\ln\left[1-\frac{T_{\mathrm{B}_0}(l,b,v)}{5.29}\left([\mathrm{e}^{5.29/T_{\mathrm{ex}}^{13}(l,b,v)}-1]^{-1}-0.16\right)^{-1}\right]. \tag{A4}$$

T_{ex}^{13} is estimated starting from the ^{12}CO $J = 1 \rightarrow 0$ transition: since in the colder region of the molecular clouds this line is optically thick, its population can be considered in LTE. It is in general a good approximation to consider the lower levels of ^{13}CO transitions in LTE within the same regions. Since the collisional and radiative transition rates per ^{13}CO molecule are very close to those of ^{12}CO, LTE implies that the relative population in the lowest ($J = 1 \rightarrow 0$) level for the two isotopes is the same (Stahler & Palla 2005). Then,

$$T_{ex}^{13} = T_{ex}^{12}. \quad \text{(A5)}$$

Equation (A2) can now be solved in the optically thick condition $\tau \gg 1$ for ^{12}CO, obtaining

$$T_{ex}^{12}(l, b, v) = T_{ex}^{13}(l, b, v) = \frac{5.53}{\ln\left(1 + \frac{5.53}{T^{12}(l,b,v)+0.837}\right)}. \quad \text{(A6)}$$

Once T_{ex}^{13} and τ^{13} are computed, from equation (A1) we estimate N^{13}CO.

APPENDIX B: CROSS-CORRELATION AMONG DIFFERENT RINGS

In this section, we show that, when the cross-correlation between rings is minimal and the standard tracers account for the total column density in a given ring, the model converges to stable results in that ring, regardless of what happens in the other rings.

In order to validate our results for Ring 1, we run two different series of tests, modifying both the ring configuration and the gas column densities. The first test demonstrates that the dust emission in Ring 1 is dominant with respect to the dust emission in the other rings; the second test shows that the results obtained for Ring 1 are independent from column density variations in the other rings. We use dust temperatures as an indicator of the quality of the result obtained from each individual test. From each set of emissivities, we estimate the dust temperature associated with each gas phase and ring configuration with a simple grey-body model. This model is less sophisticated than DustEM, given that it assumes that all the IR emission comes from dust in thermal equilibrium with the RF; however, it allows us to run a large number of tests using only the Hi-GAL wavelengths, for which dust emission is dominated by the BGs contribution. At 70 μm, we neglect the additional contributions from VSGs and PAHs.

In performing the tests, we use as a reference the dust temperatures obtained for Ring 1 for each of the gas phases by adopting the ring configuration described in Section 4.2, a spectral emissivity index $\beta = 1.9$ and a grey-body model: $T_{d,H\,I} = 19.3 \pm 1.0$ K, $T_{d,H_2} = 19.5 \pm 0.9$ K and $T_{d,H\,II} = 23.3 \pm 0.3$ K.

We run the following two sets of tests:

(1) The first type of tests aims at checking the robustness of the results as a function of the adopted ring configuration. We create two different configurations, A and B. In configuration A, we consider the extreme case of having only one single ring, obtained by the integration of all the emission along the LOS. In configuration B, we have instead two rings: Ring 1, spanning the same range of Galactocentric radii as in the standard configuration ($4.5 \leq R \leq 5.6$ kpc) and Ring 2, given by the sum of the default Rings 2, 3 and 4 ($5.6 \leq R \leq 16.0$ kpc). In configuration A, the code converges, giving positive emissivities for all the three components. In configuration B, the code converges in Ring 1 but not in Ring 2.

Table B1. Temperature, and corresponding uncertainties, of dust associated with the three gas phases in configuration A (one ring integrated along the LOS) and configuration B (two rings), Ring 1.

Gas phase	Configuration A T (K)	Configuration B T (K)
H I	12.8 ± 1.0	21.5 ± 0.6
H_2	20.1 ± 0.4	20.4 ± 0.7
H I	23.6 ± 0.7	23.5 ± 0.5

Therefore, the majority of the emission arises from the region delimited by $4.5 \leq R \leq 5.6$ kpc, allowing the convergence of the code independently from the column density underestimation in Ring 2–3–4. However, the dust temperatures are strongly influenced by the blending of gas and dust along uncorrelated LOS in both configurations. The temperature of dust associated with the three different components for Ring 1 are in Table B1. The dust emissivities associated with the H I gas phase in configuration A have very high uncertainties at all wavelengths, and the resulting temperature is very low compared to the four-ring configuration result. At the same time, the H_2 dust temperature is higher than its counterpart in the four-ring configuration. These results are consequence of the ring cross-correlation. The cold regions are mostly located in a well-defined portion of the sky (the region $7.4 \leq R \leq 8.5$ kpc, see Section 6.2), but in these tests they are blended together with the warm gas. If the cold regions are not properly isolated (i.e. the rings are not separated as in Section 4.2), the blending makes the dust in the rings, which include these features colder. To compensate for that, similarly to what happens if we ignore the ionized gas in the inversion (the warmest component, see Section 6.5), the code makes artificially warmer the other rings. In addition, since the majority of the H II gas is in Ring 1, with a minor contribution from the other rings, the emissivities and the temperature of dust associated with this phase are very similar to the four-ring configuration.

The same effect is evident in configuration B, where both H I and H_2 are warmer than their counterparts in the four-ring configuration. The blending of different H I components for $5.6 \leq R \leq 16.0$ kpc (and of H_2 components for $5.6 \leq R \leq 8.5$ kpc) prevents the convergence of the code in Ring 2 and makes artificially warmer the temperature of dust associated with H I and H_2 in Ring 1.

On the contrary, if the rings are well defined into physically independent regions, the propagation of errors across rings is minimal, as demonstrated with the second series of tests.

(2) In these tests, we fixed the four-ring configuration, and we simulate the effect of a poor column density estimation. We run nine different configurations: in each configuration we add, for each Ring 1–3 and phase of the gas, a synthetic gas column density to the gas column densities evaluated in Section 4.3.

We generate unbiased synthetic column density maps for each gas component and ring as a random Gaussian distribution with a variance equal to the dispersion of each original map. Independently from the configuration, the model always converges in Ring 1 and does not converge in Ring 2–3–4. The dust temperatures for each gas phase in Ring 1, for the nine different configurations, are in Table B2. With the exception of the altered gas phase and ring, the dust temperatures are the same, within the errors, of the reference values. Since the correlation among gas phases and rings is

Table B2. Temperature, and corresponding uncertainties, of dust associated with the three gas phases in the nine test cases described in Appendix B.

Modified ring	*Modified gas phase*	H I T(K)	H_2 T(K)	H II T(K)
Ring 1	H I	19.6 ± 1.4	18.2 ± 0.9	23.2 ± 0.3
Ring 2	H I	20.3 ± 0.7	18.8 ± 0.9	23.5 ± 0.5
Ring 3	H I	19.6 ± 0.8	18.9 ± 0.9	23.5 ± 0.3
Ring 1	H_2	19.6 ± 0.9	13.8 ± 3.6	23.4 ± 0.4
Ring 2	H_2	19.7 ± 1.1	19.0 ± 0.8	23.7 ± 0.3
Ring 3	H_2	20.1 ± 0.6	19.4 ± 1.3	23.6 ± 0.4
Ring 1	H II	20.7 ± 1.1	19.7 ± 0.7	23.2 ± 0.6
Ring 2	H II	19.3 ± 0.6	19.1 ± 1.1	23.8 ± 0.3
Ring 3	H II	19.9 ± 0.6	18.1 ± 1.1	23.8 ± 0.4

minimal in this configuration, the error in the gas column density estimation for a given ring and phase of the gas translates into a poor estimation of the emissivity associated with that ring and that phase of the gas, but it does not propagate to the other rings and gas phases.

In conclusion, the results for Ring 1 are robust and are not affected, within the inversion model errors, by even severe gas column density underestimations occurring in Rings 2, 3 and 4.

APPENDIX C: MASKING THE W43 REGION

In this section, we demonstrate that the emissivities obtained in Section 6.1 are representative of SDPF1 as a whole and are not biased by specific features present in the field, such as the bright H II region W43. In Fig. C1, we show the comparison between the default mask used in the inversion (left-hand panel) and a new mask that entirely covers W43 (right-hand panel). This new mask was generated for the purpose of investigating the robustness of the results described in the paper. The pixel size of these masks is 4 arcmin. The masked pixels are highlighted in white in the figure. In the default mask, these pixels correspond to H I 21 cm line emission associated with strong continuum emission, in correspondence of bright H II regions, as discussed in Section 3.2.1. The W43 region is already partially masked. The extended mask (Fig. C1, right-hand panel) covers a squared region with a side of $\simeq 0.^{\circ}7$ centred on W43. This mask reduces the number of good pixels from 680 to 593, a number that still assures the convergence of the code.

The emissivities associated with Ring 2–3–4 are still negative or poorly constrained, as showed in Table C1. Also the dust temperature and dust grain abundances for all the three gas phases in Ring 1 are not significantly affected by the extended mask. The DustEM fit obtained with this new set of emissivities are in Fig. C2 . They are in agreement within the errors with the main results described in Section 6.1.

This test evidences the unbiased nature of our results and stresses that the main limitation in recovering the dust emissivities in SDPF1 relies on our inability to accurately reproduce the gas content along each LOS across the field.

Table C1. Emissivities, and corresponding uncertainties, of dust associated with the three gas phases in Ring 1–2–3–4 evaluated applying to the data the extended W43 mask showed in Fig. C1, right-hand panel. The overall behaviour does not differ sensibly from the main results and in particular the emissivities associated with Ring 2–3–4 are still negative or poorly constrained by the model.

Band (μm)	ϵ_ν [MJy sr^{-1} (10^{20} H atoms cm^{-2})$^{-1}$]											
	H I				H_2			H II				
	Ring 1	*Ring 2*	*Ring 3*	*Ring 4*	*Ring 1*	*Ring 2*	*Ring 3*	*Ring 1*	*Ring 2*	*Ring 3*
8	0.757 ± 0.152	0.022 ± 0.153	-1.598 ± 0.558	0.022 ± 0.093	0.020 ± 0.019	0.079 ± 0.029	0.106 ± 0.156	0.147 ± 0.023	0.024 ± 0.043	-0.011 ± 0.226
24	0.309 ± 0.081	0.158 ± 0.094	-0.782 ± 0.466	0.090 ± 0.066	-0.001 ± 0.014	-0.025 ± 0.038	0.048 ± 0.044	0.134 ± 0.027	0.156 ± 0.032	0.117 ± 0.147
70	3.346 ± 1.209	2.435 ± 1.153	-8.288 ± 6.892	-3.837 ± 1.216	0.286 ± 0.230	-0.853 ± 0.684	2.008 ± 0.582	2.659 ± 0.254	2.720 ± 0.899	3.822 ± 2.283
160	12.699 ± 3.598	4.796 ± 2.359	-14.850 ± 13.388	-16.719 ± 4.120	1.528 ± 0.363	1.909 ± 2.041	0.926 ± 2.046	6.197 ± 0.793	4.207 ± 2.264	8.744 ± 5.098
250	11.626 ± 1.826	2.726 ± 2.942	-23.089 ± 9.234	-7.821 ± 1.859	1.331 ± 0.218	2.137 ± 0.913	-2.851 ± 1.626	3.299 ± 0.568	0.289 ± 0.626	3.975 ± 3.674
350	4.916 ± 0.514	1.174 ± 1.050	-6.294 ± 1.286	-3.067 ± 0.961	0.528 ± 0.069	0.633 ± 0.472	-1.072 ± 0.553	1.170 ± 0.198	0.348 ± 0.553	2.119 ± 0.714
500	1.771 ± 0.203	0.299 ± 0.488	-2.807 ± 0.824	-0.825 ± 0.236	0.206 ± 0.022	0.239 ± 0.177	-0.431 ± 0.187	0.411 ± 0.033	0.074 ± 0.184	0.933 ± 0.522

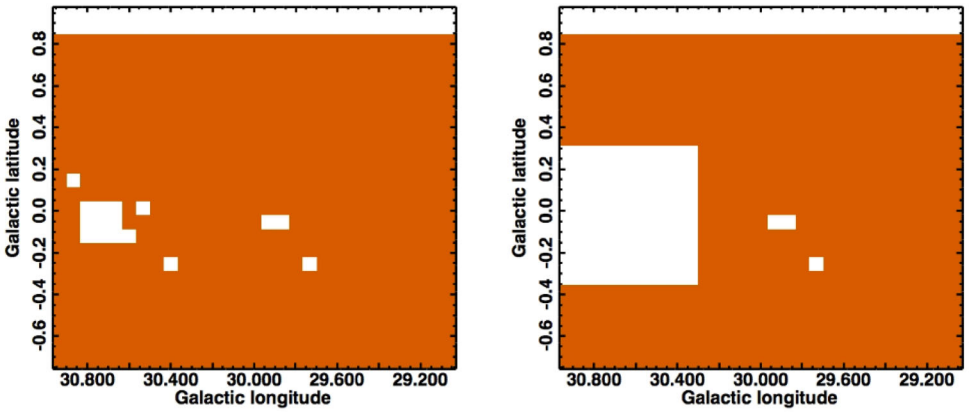

Figure C1. *Left*: mask used in the main run at the final working resolution of 14.8 arcmin and a pixel size of 4 arcmin. The white pixels are the flagged pixels and they are mainly in correspondence of the strong continuum H I emission observed along bright H II regions LOS, as discussed in Section 3.2.1. *Right*: the mask used in the test described in Section C. It is a square with a side of 0.°7 and it fully encompass the W43 region.

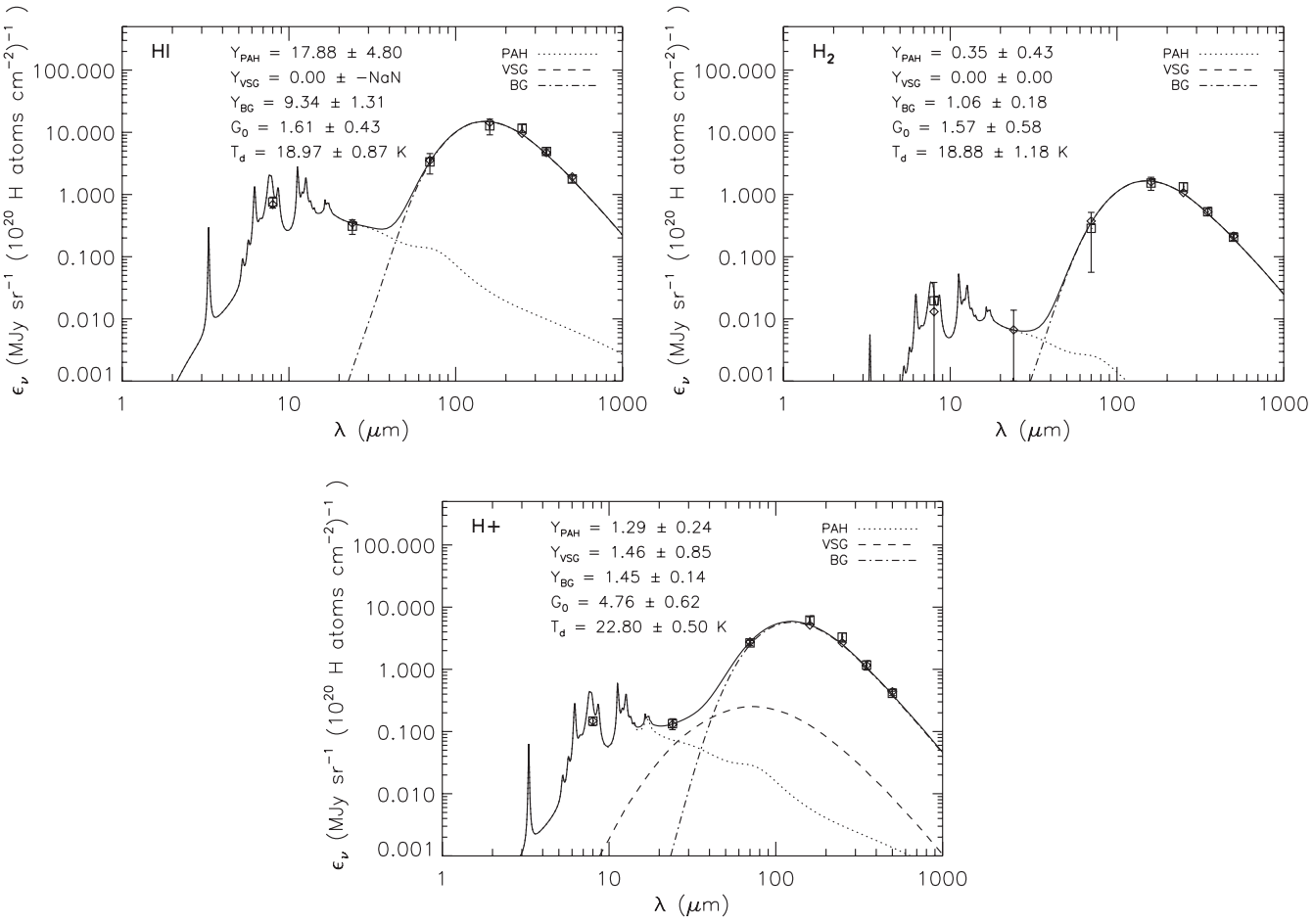

Figure C2. DustEM fit of the emissivities in Table C1 using the W43 extended mask for the three gas phases in Ring 1. The dust temperatures and dust grain abundances are in agreement within the errors with the main results described in Section 6.1 using the default mask showed in Fig. C1.

APPENDIX D: INPUT AND COLUMN DENSITY MAPS

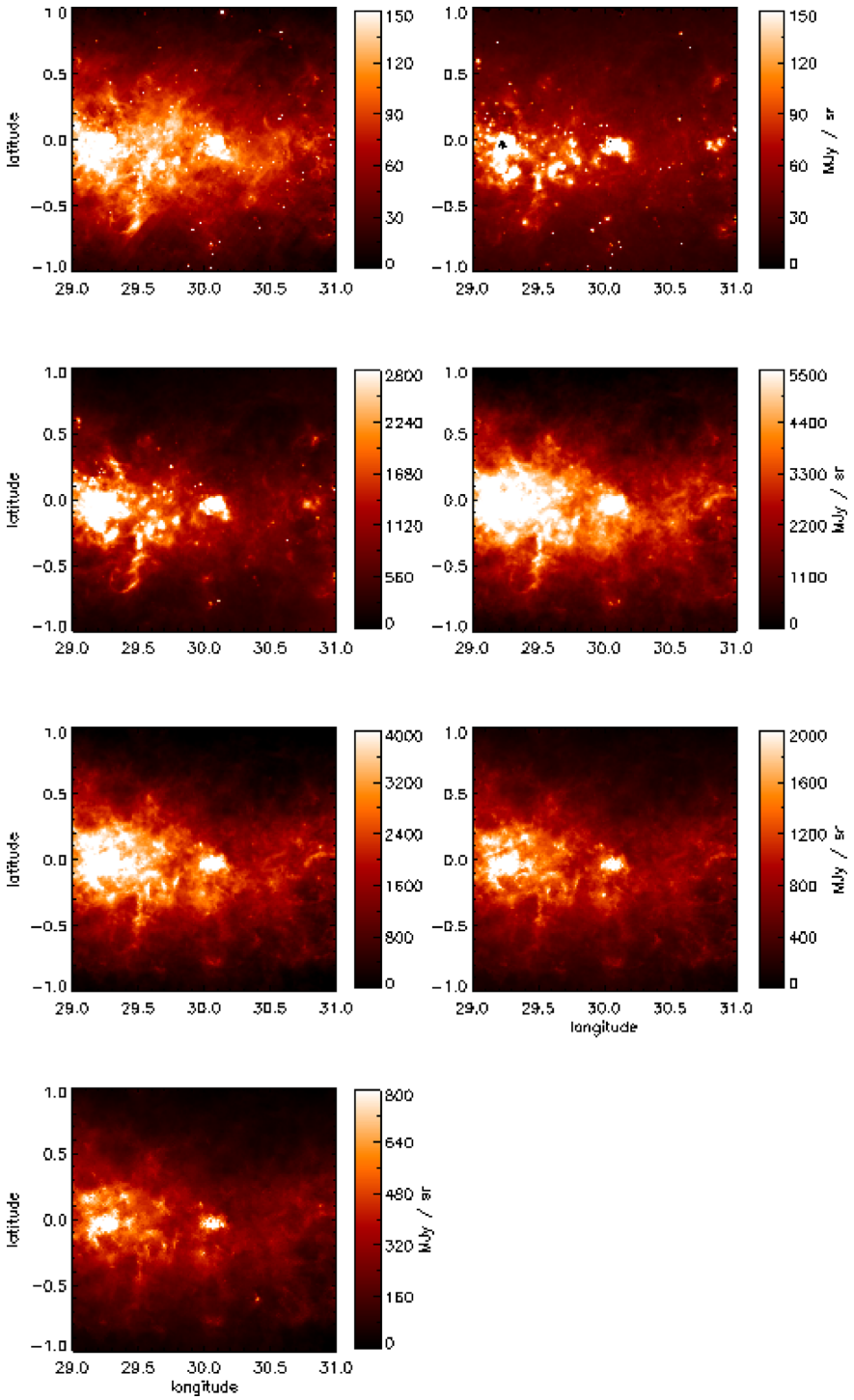

Figure D1. IR maps used as input in equation (1). From the top to the bottom, left to right: IRAC 8 μm, MIPS 24 μm, PACS 70 and 160 μm, SPIRE 250, 350 and 500 μm. All maps have been calibrated in MJy sr^{-1} and point-source subtracted as described in Section 3.1.

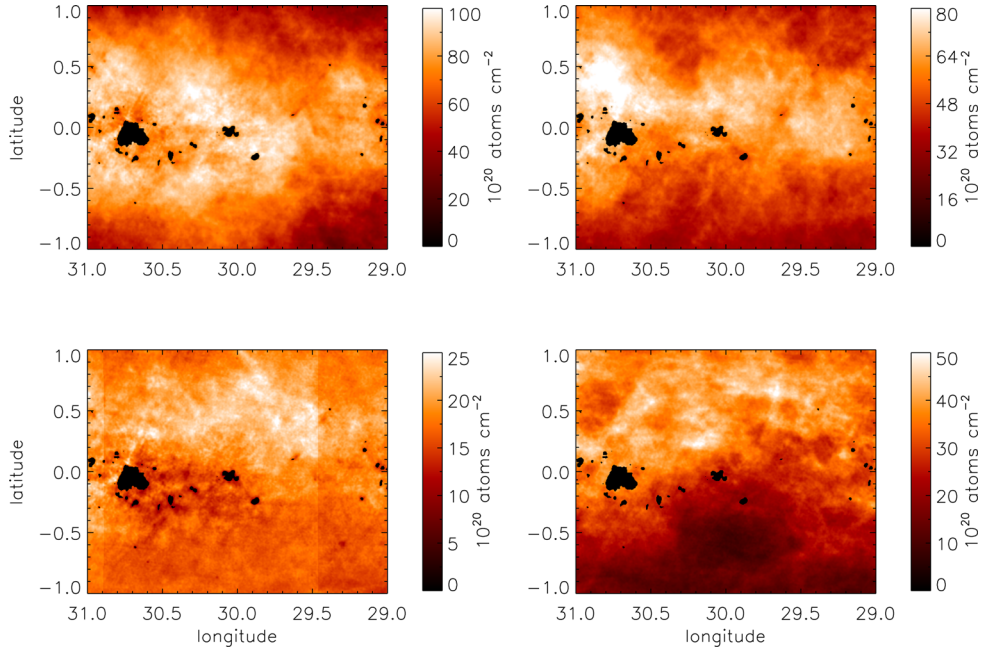

Figure D2. H I column density maps in Ring 1 (upper left), Ring 2 (upper right), Ring 3 (lower left) and Ring 4 (lower right) at native VGPS angular resolution (1 arcmin). The black pixels are the masked pixels in correspondence of strong continuum emission (see Section 3.2.1). The steps in Ring 3 around $l = 29.^{\circ}5$ and $l = 30.^{\circ}8$ are at the longitudes in which the emission is split among Rings 2 and 3, and it is of $\simeq 1 \times 10^{20}$ H atoms cm^{-2}. The same steps are indeed present in Ring 2, but they are not visible in the map.

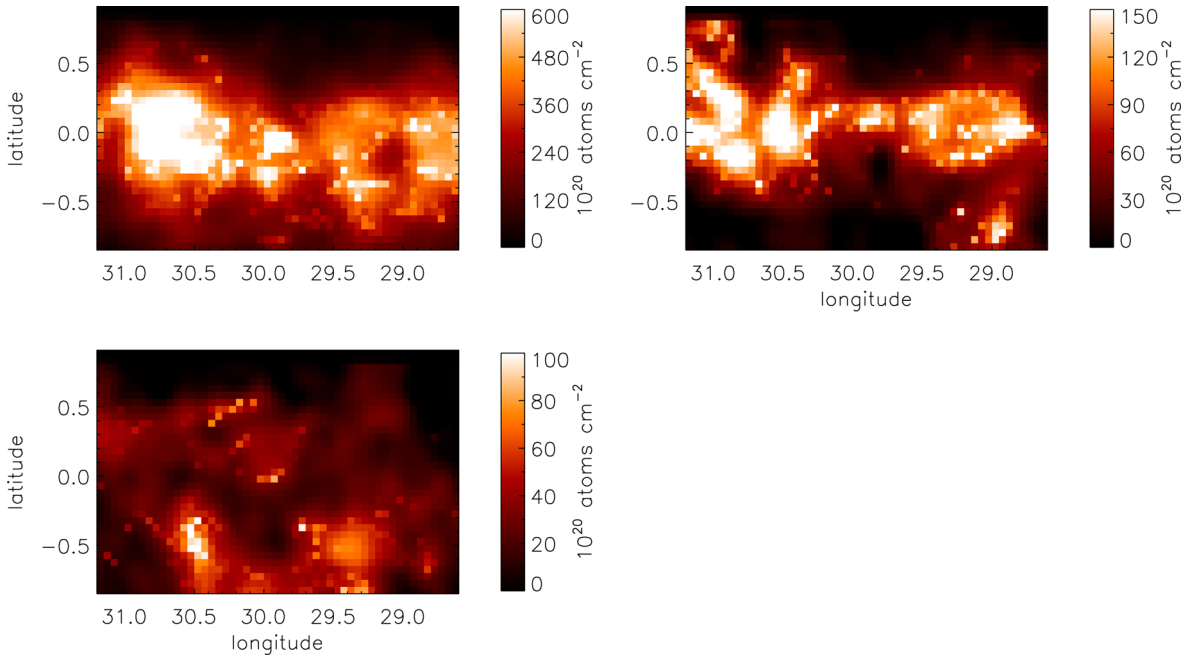

Figure D3. H_2 column density maps in Ring 1 (upper left), Ring 2 (upper right) and Ring 3 (lower left). The bright pixels are in correspondence of high column density regions where both ^{12}CO and ^{13}CO emission have been observed. The resolution is 9 arcmin with a pixel scale of 3 arcmin, obtained combining ^{12}CO and ^{13}CO data sets (see Section 3.2.2).

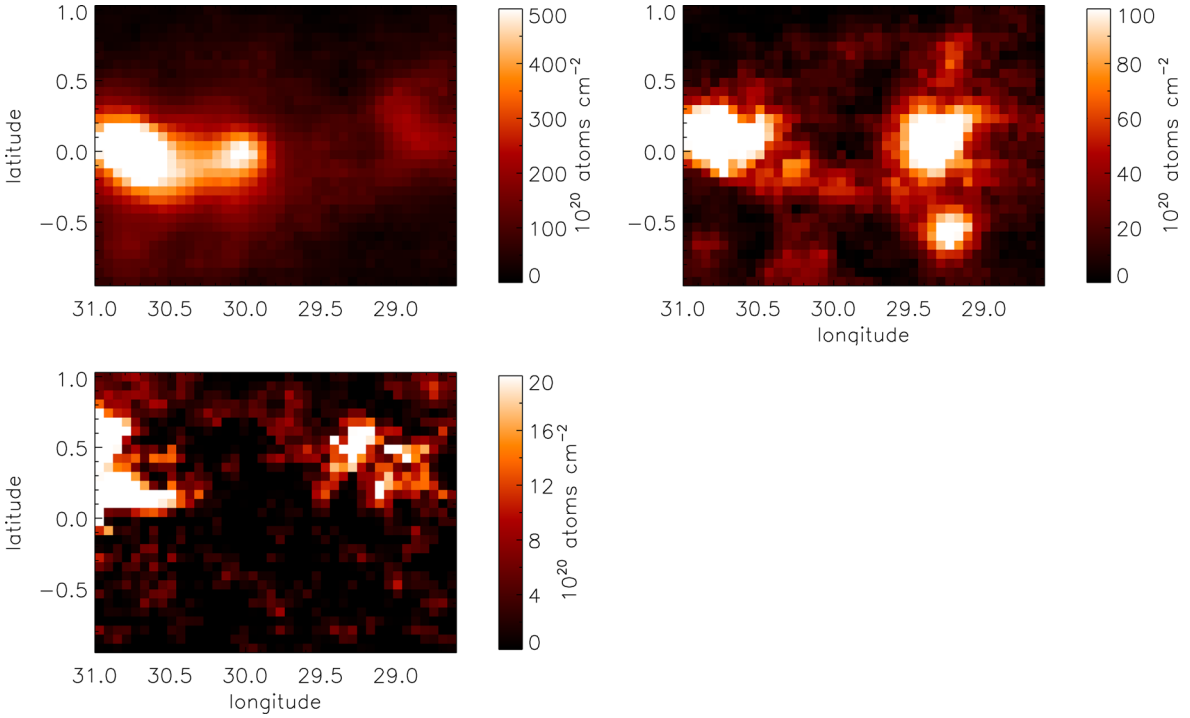

Figure D4. H I column density maps in Ring 1 (upper left), Ring 2 (upper right) and Ring 3 (lower left). The majority of the ionized gas is in Ring 1, in correspondence of W43 complex. The map resolution is 14.8 arcmin.

This paper has been typeset from a TEX/LATEX file prepared by the author.